JCB Journal of Cell Biology

ARTICLE

Nano-scale resolution of native retinal rod disk membranes reveals differences in lipid composition

Christopher L. Sander[1,2], Avery E. Sears[1,2], Antonio F.M. Pinto[3], Elliot H. Choi[1,2], Shirin Kahremany[2], Fangyuan Gao[2], David Salom[2], Hui Jin[1], Els Pardon[4,5], Susie Suh[1,2], Zhiqian Dong[2], Jan Steyaert[4,5], Alan Saghatelian[3], Dorota Skowronska-Krawczyk[2,6], Philip D. Kiser[2,6,7], and Krzysztof Palczewski[2,6,8]

Photoreceptors rely on distinct membrane compartments to support their specialized function. Unlike protein localization, identification of critical differences in membrane content has not yet been expanded to lipids, due to the difficulty of isolating domain-specific samples. We have overcome this by using SMA to coimmunopurify membrane proteins and their native lipids from two regions of photoreceptor ROS disks. Each sample's copurified lipids were subjected to untargeted lipidomic and fatty acid analysis. Extensive differences between center (rhodopsin) and rim (ABCA4 and PRPH2/ROM1) samples included a lower PC to PE ratio and increased LC- and VLC-PUFAs in the center relative to the rim region, which was enriched in shorter, saturated FAs. The comparatively few differences between the two rim samples likely reflect specific protein–lipid interactions. High-resolution profiling of the ROS disk lipid composition gives new insights into how intricate membrane structure and protein activity are balanced within the ROS, and provides a model for future studies of other complex cellular structures.

Introduction

Rod photoreceptor cells of the retina are highly differentiated neurons that transduce visible light into a biochemical signaling cascade. These cells have an elongated cilium called the rod outer segment (ROS), which is composed of an internal stack of membranous disks surrounded by plasma membrane (PM). Two proteins are required to form the unique membrane structure: the light-receptive protein rhodopsin and a structural protein complex known as peripherin2-ROS membrane protein 1 (PRPH2/ROM1), which is essential for maintenance of the curved, bulbous rim of ROS disks (Goldberg and Molday, 1996a, b; Loewen and Molday, 2000; Kevany et al., 2013; Zulliger et al., 2018; Milstein et al., 2020). Roughly 40 million molecules of rhodopsin are packed into each ROS, and each light-activated rhodopsin is capable of binding and activating many molecules of the G protein transducin (Fung et al., 1981; Nathans, 1992; Polans et al., 1996; Heck and Hofmann, 2001). A third protein critical for photoreceptor function is the ATP-binding cassette (ABC) protein, family A, number 4 (ABCA4), which resides in the disk rim, like PRPH2/ROM1, and assists in retinaldehyde clearance from the ROS disk through its *N*-retinylidene-phosphatidylethanolamine flippase activity.

To accommodate this dynamic yet structured environment, ROS disks contain specialized lipids rich in long chain and very long chain polyunsaturated fatty acids (LC-PUFAs and VLC-PUFAs, respectively; Rotstein and Aveldaño, 1988). The location of these VLC–fatty acids (FAs) within the disk membrane interior or the disk rim membranes has become a point of debate in the field. VLC-PUFAs were hypothesized to provide flexibility in the disk membrane interior by folding back on themselves on one side of the bilayer (McMahon and Kedzierski, 2010; Molday and Zhang, 2010). This hypothesis was strengthened by findings that showed LC- and VLC-PUFAs remained with rhodopsin after hexane extraction of photoreceptor membranes (Aveldaño, 1988). Furthermore, rhodopsin exhibits maximal activity in a phospholipid environment with a high proportion of the VLC-PUFA, docosahexaenoic acid (DHA; 22:6; Mitchell et al., 1992). A subsequent theory suggested that because (1) elongation of VLC-FA protein 4 (ELOVL4) is responsible for VLC-PUFA production and (2) ELOVL4 and ABCA4 mutations both cause Stargardt

[1]Department of Pharmacology, Case Western Reserve University, Cleveland, OH; [2]Department of Ophthalmology, Gavin Herbert Eye Institute, University of California, Irvine, Irvine, CA; [3]Clayton Foundation Laboratories for Peptide Biology, Salk Institute for Biological Studies, La Jolla, CA; [4]Vlaams Instituut voor Biotechnologie–Vrije Universiteit Brussel Center for Structural Biology, Vlaams Instituut voor Biotechnologie, Brussels, Belgium; [5]Structural Biology Brussels, Vrije Universiteit Brussel, Brussels, Belgium; [6]Department of Physiology and Biophysics, University of California, Irvine, Irvine, CA; [7]Research Service, VA Long Beach Healthcare System, Long Beach, CA; [8]Department of Chemistry, University of California, Irvine, Irvine, CA.

Correspondence to Krzysztof Palczewski: kpalczew@uci.edu; Philip D. Kiser: pkiser@uci.edu; Dorota Skowronska-Krawczyk: dorotask@uci.edu.

disease (STGD3 and 1, respectively), VLC-PUFAs may reside in the ROS disk rims and affect ABCA4 activity, providing a potential link between two Stargardt mutations (Agbaga et al., 2010).

The disks are also known to have significantly higher levels of phosphatidylethanolamine (PE) than are typically found in PMs (Boesze-Battaglia and Albert, 1992; Daemen, 1973), which is compensated by a relative scarcity of phosphatidylcholine (PC) and phosphatidylserine (PS) in ROS membranes. This unusual phospholipid distribution is of functional importance as ABCA4 is optimally active when the membrane contains at least 40% PE (Sun and Nathans, 2001; Quazi and Molday, 2013; Quazi et al., 2012). Cholesterol has also been found to be necessary for rhodopsin activity, although high concentrations reduce its signaling efficiency (Mitchell et al., 1990, 1992; Palczewski, 2006). Indeed, many components of the membrane can have a profound impact on the function of the membrane proteins therein, making high-resolution study of membrane environments critical to the overall characterization of membrane proteins (Zimmerman and Keys, 1989; Bush et al., 1991; Gibson and Brown, 1993; Suh et al., 1994; Albert et al., 1998; Agbaga et al., 2008; Berdeaux et al., 2010; Giusto et al., 2010; Bennett et al., 2014; Gorusupudi et al., 2021; Hamano et al., 2021). Early work by Falk and Fatt (1969) on the ultra-structure of ROS membranes showed a remarkable ability of the outer rim region of ROS disks to resist disruption after OsO_4 fixation. Their work indicated that membranes in the rim region are distinct from the disk center, but concrete evidence in support of this idea is lacking.

The current paucity of knowledge regarding molecular differences between the center and rim regions of ROS disk membranes represents a significant bottleneck in the study of lipid synthesis, metabolism, and transport (Zhang et al., 2001; Edwards et al., 2001; Chen et al., 2005, 2007; Berdeaux et al., 2010; Sapieha et al., 2011; Chen et al., 2013, 2020). These processes modulate the impact of lipids on retinal degenerative diseases, such as STGD3, retinitis pigmentosa, diabetic retinopathy, and age-related macular degeneration (Simonelli et al., 1996; Bernstein et al., 2001; Seddon et al., 2003, 2006; SanGiovanni et al., 2007; Liu et al., 2010; Tikhonenko et al., 2010, 2013; Logan et al., 2013; Logan and Anderson, 2014; Hiebler et al., 2014). Mapping the possible lipid domains in which vision-related membrane proteins reside would be an invaluable contribution to the study of protein–lipid interactions.

The advent of styrene maleic acid (SMA) lipid particles (SMALPs) has made it possible to directly extract the membrane bilayer into discrete membrane disks containing the proteins therein (Knowles et al., 2009; Jamshad et al., 2011). It was initially unclear whether lipids "copurified" with native proteins represent the environment from which the protein was extracted. Accordingly, there have been reports on the lipid exchange dynamics of polymer-bound lipid nanodiscs (Cuevas Arenas et al., 2017; Schmidt and Sturgis, 2018; Danielczak and Keller, 2018). Initial studies showed that phospholipids extracted in SMALPs and diisobutylene maleic acid lipid particles can exchange more rapidly at ambient temperatures (i.e., 20–30°C) as compared with those prepared in large unilamillar vesicles or membrane scaffold protein nanodiscs. These findings suggested that native membrane proteins, once extracted by SMA, might reside in a lipid environment that reflects the average lipid environment of the extracted tissue. However, more recent data have provided evidence that SMALPs of various bacterial proteins formed under lower temperature conditions (≤4°C) have distinct lipid profiles (Teo et al., 2019), indicating the native local membrane environment composition is retained in samples prepared in this manner (local meaning a spatial resolution of 10–11 nm in diameter).

Here, we apply the SMA extraction method to enable detergent-free purification of functional rhodopsin, ABCA4, and PRPH2/ROM1 lipoprotein particles from bovine ROS disk membranes (Fig. 1, a and b). Untargeted lipidomic analysis of these samples reveals key differences in lipid composition between the central and rim regions of the disk that are likely of structural and functional importance.

Results

SMA extraction of ROS membrane proteins and development of mAb against ABCA4

We began by analyzing the ability of SMA to solubilize components of the ROS (Fig. 1). SMA showed a strong capacity for extracting ROS membrane proteins (Fig. S1 a). The high yield of total protein obtained from ROS extracted in SMA also showed near-complete extraction of the available ABCA4, as shown by immunoblot analysis (Fig. S1 b). Optimum extraction of ABCA4 in SMA occurred at 2.5% wt/vol and was essentially complete; by contrast, 2% laurel maltose neopentyl glycol (LMNG; roughly 2,000× the critical micelle concentration) resulted in roughly 50% solubilization.

The C-terminal region of ABCA4 contains a high-affinity binding epitope for the Rim3F4 antibody (YDLPLHPRT; Illing et al., 1997). The Rim3F4 antibody has high affinity for the C terminus of ABCA4, but immunopurification of ABCA4 proved difficult, given the low efficiency of elution from the column. We circumvented this limitation by generating a novel ABCA4 mAb (CL2), which was developed against a 26–amino acid peptide found at the C terminus of bovine ABCA4. Fig. S1 c shows the location and length of the resultant antibody binding site for CL2, in comparison to the locations of the antibody binding sites for Rim3F4 and TMR4 (Zhang et al., 2015), another antibody that targets the second extracytosolic domain. Dot blot analysis of CL2 confirmed that the paratope was different from that of Rim3F4 (Fig. S1 d). CL2 generated a reduced signal in the immunoblot of solubilized bovine ROS (Fig. S1 f), indicative of lower-affinity binding to the antigen.

The relatively weak binding of CL2 to ABCA4 was also apparent in murine samples (Fig. S1, e and g). The immunohistochemical analysis of murine retinas showed a gradual increase in ABCA4 signal intensity in samples stained with higher concentrations of CL2 (Fig. S1 e). CL2 showed a level of signal comparable to that of Rim3F4 for the same murine samples via immunoblots with comparable specificity (Fig. S1 g).

Detergent-free purification of ABCA4 with CL2 antibody and EM imaging

SMA-extracted bovine ROS was incubated with CL2-conjugated immunoaffinity resin (Fig. 1 c). Elution of ABCA4 with the

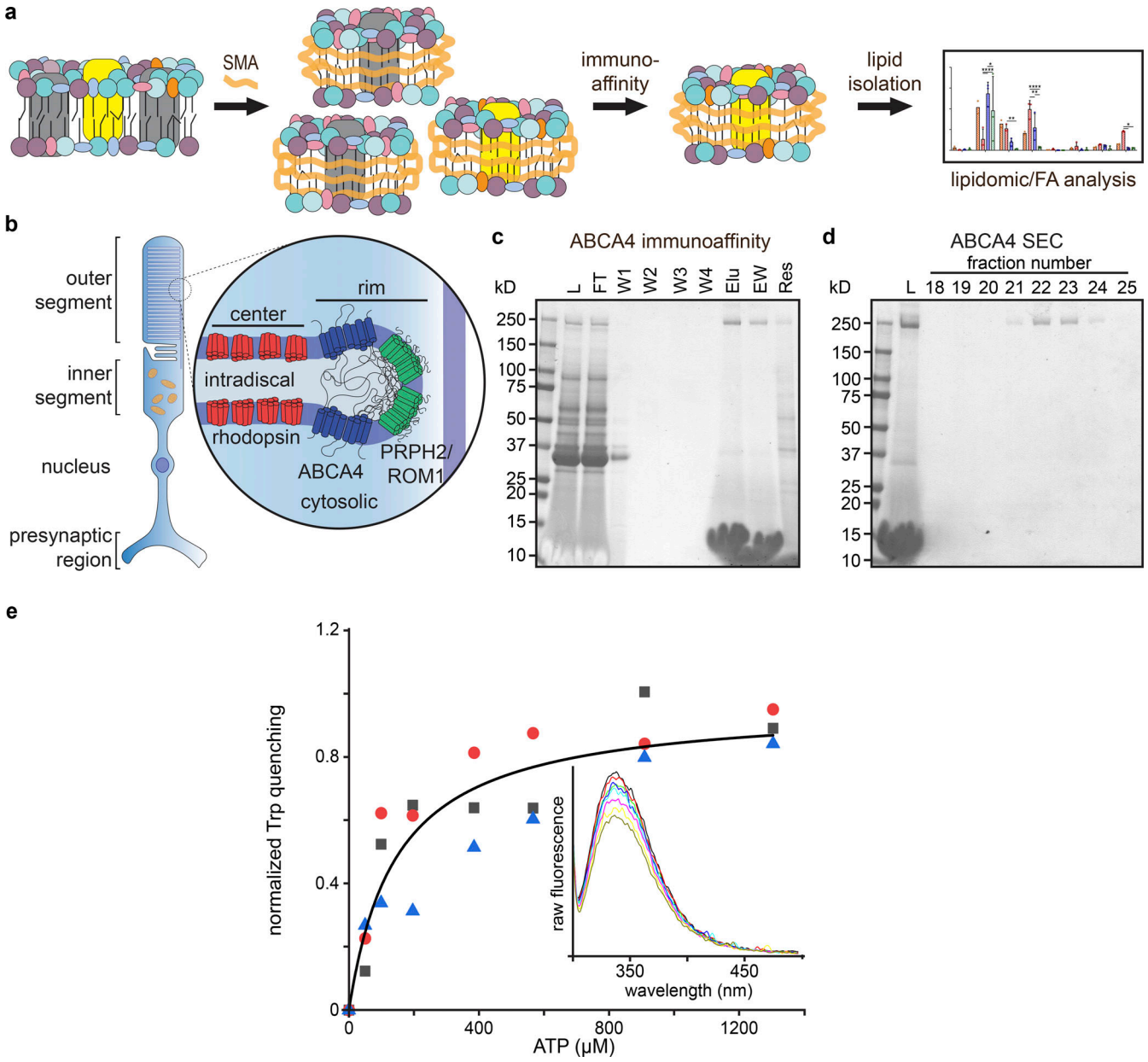

Figure 1. **Detergent-free purification of native ABCA4 from bovine ROS by immunoaffinity chromatography. (a)** Native lipids isolated by the SMALP coimmunopurification procedure. SMA extracts membrane proteins with their native lipids; the SMALPs may then be subjected to immunoaffinity chromatography for purification of native nanodiscs, enabling analysis of copurifying lipids. **(b)** The intricate membrane structure of ROS disks in rod photoreceptors. Three major membrane protein components are rhodopsin, ABCA4, and PRPH2/ROM1. **(c)** Detergent-free, immunoaffinity purification of ABCA4 using the CL2 mAb. L, soluble ROS (16 ml, 10 µl loaded); FT, flow-through (16 ml, 10 µl loaded); W1-4, washes 1–4 (each 15 ml, 10 µl loaded); Elu, elution (1 ml, 10 µl loaded); EW, wash of column after elution (1 ml, 10 µl loaded); Res, resin (1 ml, 10 µl loaded). Stained with Coomassie Blue R250. **(d)** Detergent-free SEC of combined elution fractions, 18–25 fraction numbers, 0.5 ml fractions from SEC, 10 µl loaded per lane. Stained with Coomassie Blue R250. **(e)** ABCA4 extracted and purified in SMALPs shows intrinsic Trp-quenching characteristic of ATP transporters in the presence of serially added ATP (dissociation constant [K_d] = 133.5 µM). Three separate experiments are shown with different symbols. Langmuir binding isotherm curve (black) fit to the average of three runs (maximum quench [Q_{max}] = 11.85%, 17.91%, and 10.00% for black, red, and blue, respectively). Inset: One set of spectra for increasing concentrations of ATP, showing diminution of raw fluorescence.

known epitope peptide produced a concentrated and pure sample of ABCA4 (Fig. 1 c, "Elu" and "EW" lanes), with large amounts of elution peptide and characteristic SMA smearing seen at the bottom of these lanes. The elution and subsequent wash from the immunoaffinity purification were then pooled and concentrated for size exclusion chromatography (SEC; Fig. 1 d). To characterize possible morphological changes to ABCA4 in the SMALP, the purified samples were prepared for negative stain transmission EM (nsTEM), which showed monodisperse, homogenous ABCA4 particles (Fig. S1 h, left). Clear 2D class averages were generated from particles selected by an unbiased autopicking feature of computational imaging system for

transmission electron microscopy (cisTEM; Fig. S1 h, right; Grant et al., 2018). The resultant de novo 3D model, obtained using the cisTEM's de novo reference map generator, showed significantly more density in the transmembrane domain (TMD) region than the prior nsTEM-generated structure of ABCA4 (Fig. S1 i). After refining, the roughly 4-nm-thick TMD showed a diameter of roughly 12 nm, which was larger than the previously published nsTEM model in the presence of detergent (EMDB-5497, orange; Fig. S1 j; Tsybovsky et al., 2013). The increased density did not confirm the presence of lipids in the TMD, and the possibility existed that more stain could have adhered to the TMD of the SMA-extracted protein. When considered in light of all of the results reported herein, however, we suspect the increased density was due to copurifed lipids. The other proportions obtained agreed well with the published ABCA4 nsTEM model and the general size and shape of ABCA1 (EMDB-6724, purple ribbon; Fig. S1, i and j; Qian et al., 2017).

Assessing the activity of ABC transporters in SMA presents a challenge because the low millimolar concentrations of magnesium preferred for efficient coordination of ATP to the Walker A binding site of ABC transporters precipitates SMA (Oluwole et al., 2017). The correct folding and nucleotide binding of ABC transporters in SMALPs can be assessed via tryptophan fluorescence quenching with increasing concentrations of ATP in the absence of magnesium (Gulati et al., 2014). Using this assay, we confirmed that the SMA-purified ABCA4 is able to bind ATP (dissociation constant = 133.5 μM), albeit with lower affinity than reported in the presence of magnesium (Fig. 1 e; Ahn et al., 2000).

Detergent-free purification of PRPH2/ROM1 with novel nanobody Nb19

We developed a novel nanobody to pulldown PRPH2/ROM1 via an added His_6 tag on the nanobody (Fig. 2). All nanobodies share similar topology; they primarily vary in the hinge regions (H1, H2, etc.), which, upon folding, create complementarity-determining regions that constitute the paratope (Fig. 2, a–c). We selected, purified, and expressed 5 Nbs (Nb13, Nb19, Nb20, Nb28, and Nb32) representing different sequence families, each family grouped by complementarity-determining region sequences (Fig. 2, b and d; Pardon et al., 2014). All of the nanobodies bound tightly to prepurified PRPH2/ROM1 as monitored by SEC (Fig. 2 e). Nb19 proved to be the most efficient binder, as immunoprecipitation of PRPH2/ROM1 from extracted ROS (using the His_6 tag on the nanobody to bind Ni^{2+}-nitrilotriacetic acid resin) gave the highest yield (Fig. 2 f). The resulting PRPH2/ROM1-Nb19 complex was of sufficient purity after elution from Ni^{2+}-resin to analyze its copurifying lipids directly (Fig. 2, g and h).

SMALP-encapsulated rhodopsin retains ligand binding capacity

Rhodopsin is by far the most abundant membrane protein found in the central region of the ROS disk membrane, making it an excellent target protein to probe the lipid composition of the disk interior. Although rhodopsin is also found in the PM of the ROS, this represents a negligible fraction of total rhodopsin (i.e., <2%) that would not complicate its use to probe the lipid composition of the central disk (Kessler et al., 2014). We assessed the ability of rhodopsin to be purified in SMA with retention of bleaching and regeneration capacity (Fig. 3). Rhodopsin was purified using the 1D4 antibody that had been developed previously and is well-established for protein purification in detergent-solubilized conditions (Fig. 1 g). SMA-solubilized rhodopsin purified by 1D4 immunoaffinity chromatography (Molday and Molday, 2014) retained its chromophore when maintained in the dark, which suggested that the protein was structurally preserved. Moreover, SMA-purified rhodopsin could be photobleached, with and without hydroxylamine to scavenge the chromophore, showing that the protein either has sufficient free volume or the SMALP has enough flexibility to allow rhodopsin conformational changes required for these processes. The apo-opsin protein could also be regenerated efficiently with 9-cis-retinal, as shown by the reappearance of the characteristic absorbance peak of the opsin-chromophore complex at 487 nm (Hubbard and Wald, 1952). The regenerated samples were stable and soluble for days at room temperature. These results highlight the ability of SMALPs to efficiently extract this model G protein–coupled receptor (GPCR) in a stable form from its native, mammalian tissue, as has been done with other GPCRs (Bada Juarez et al., 1862; Jamshad et al., 2015; Gakhar et al., 2020; Ganapathy et al., 2020; Routledge et al., 2020; Ueta et al., 2020).

Untargeted lipidomic analysis of native SMALPs reveals different membrane environments for ABCA4, PRPH2/ROM1, and rhodopsin

With SMALP-extracted, immunopurified samples of these three representative membrane proteins in hand, we performed a high-resolution study of the lipid environments of each protein. Lipidomic analysis indicated that the SMALPs were able to extract many lipid classes from native ROS membranes, including phospholipid derivatives and other membranous lipid molecules in addition to phospholipids (Figs. 4, 5, S2, S3, S4, and S5). We detected many metabolites and other lipids, including acylcarnitines (AcCa), ceramides (Cer), cholesterol esters, monoacylglycerols, diacylglycerols, triacylglycerols, free FAs (FFAs), cardiolipin, and several lyso-phospholipids (lyso-PLs: lyso-phosphatidylcholine [LPC], lyso-phosphatidylethanolamine [LPE], and lyso-phosphatidic acid). There were many distinctions in the relative species composition within these lipid classes. In general, we observed the samples of SMA-extracted ROS (starting material) and rhodopsin had similar compositions (as would be expected given the large share of the ROS occupied by rhodopsin). Likewise, we found that the SMALPs of ABCA4 and PRPH2/ROM1, which both reside in the rim region, had similar species distributions within each lipid class. As a percentage of the total lipid class, the samples from the rim region lacked AcCa(16:0), which was balanced by a relative enrichment of AcCa(22:4) (Fig. 4 a). There was no gradual increase in the chain lengths up to AcCa(22:4) in the rim samples, suggesting that free carnitine becomes conjugated to the 22:4 FA directly, and that the resultant AcCa(22:4) is not metabolized as quickly as species of similar length. The

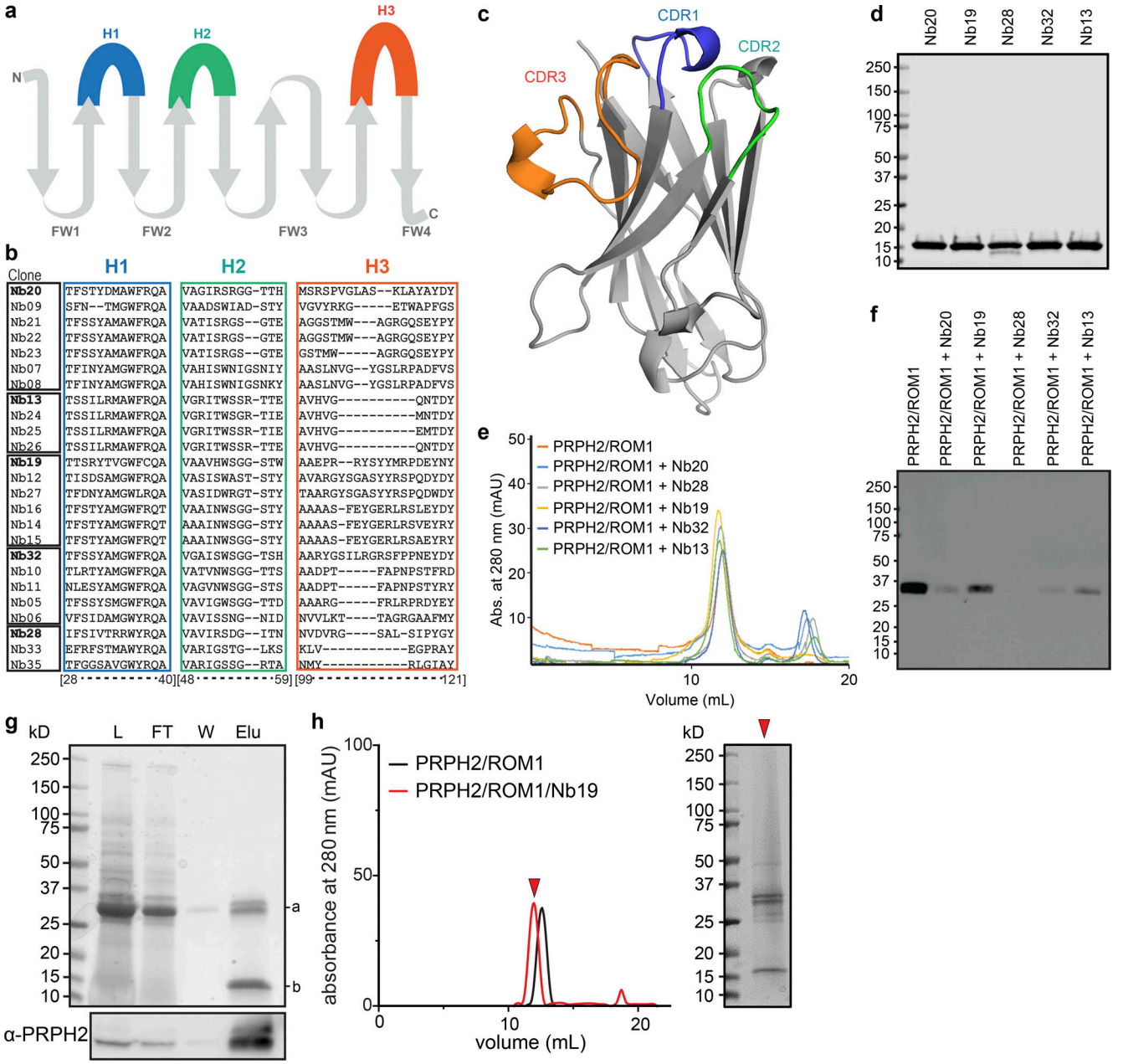

Figure 2. **Biochemical characterization and purification of the SMALP-encapsulated PRPH2/ROM1/Nb19 complex. (a)** The secondary structure of the Nb domain consists of nine β sheets separated by loop regions. H1, H2, and H3 are separated by four framework (FW) regions. **(b)** Each of the five delineated Nb families is defined by boxes around the clone names. Hypervariable region sequences H1, H2, and H3 are listed after each clone name and boxed in blue, green, and orange, respectively. **(c)** Robetta-homology modeled Nb19 is shown, highlighting extended complementarity-determining regions (CDRs) encoded by hypervariable regions defined in b. **(d)** 10 µg of purified Nb20, Nb19, Nb28, Nb32, and Nb13 were subjected to SDS-PAGE (stained with Coomassie Blue R250). **(e)** 10 µg of PRPH2/ROM1 was subjected to Superdex-200 gel filtration alone or after incubation with 20 µg of Nb. Nb19 caused the greatest shift in volume of elution. **(f)** Immunoprecipitation of PRPH2/ROM1 from solubilized ROS with Nbs. First lane, purified PRPH2/ROM1 (1.0 µg), was used as a positive control. Detection of PRPH2/ROM1 was performed by immunoblotting with the C6 (anti-PRPH2) and 2H5 (anti-ROM1) antibodies. Nb19-mediated immunoprecipitation produced the greatest quantity of PRPH2/ROM1. **(g)** Detergent-free, immunoaffinity purification of PRPH2/ROM1 (a) using the Nb19 nanobody (b). L, soluble ROS (10 ml, 10 µl loaded); FT, flow-through (10 ml, 10 µl loaded); W, wash (10 ml, 10 µl loaded); Elu, elution (2.5 ml, 2.5 µl loaded). Bottom: Anti-PRPH22 immunoblot of the above samples. **(h)** Detergent-free size exclusion chromatography of combined elution from Nb19-immunoaffinity purification. Left: PRPH2/ROM1 incubated with Nb19 (red) elutes earlier than PRPH2/ROM1 alone (black). Right: Peak PRPH2/ROM1/Nb19 fraction run on SDS-PAGE and stained with Coomassie Blue R250. Abs., antibodies; mAU, milliArbitrary Units.

rim samples showed a relative abundance of Cer(d18:1_18:0) as compared with the rhodopsin samples, whereas the rhodopsin samples showed a relative abundance of Cer(d18:1_22:0), Cer(d18:1_24:1), and Cer(d18:2_24:0), suggesting a preference for longer chain lengths (Fig. 4 b). The same relative preferences were seen with LPC and LPE analyses. The rim samples showed significant enrichment in LPC(18:0) and LPE(18:0), while LPC(22:5) and LPE(22:5), as well as LPC(22:6) and LPE(22:6), were several-fold

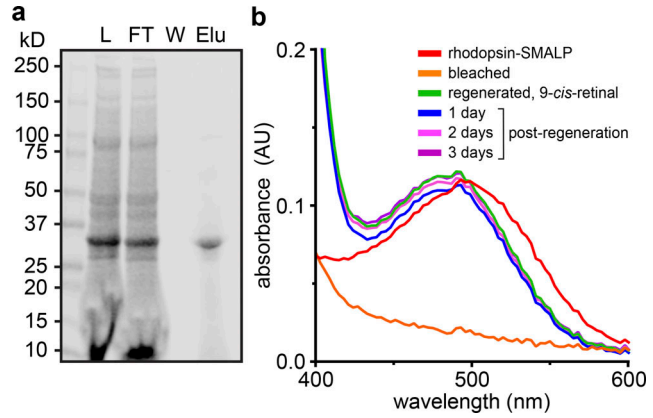

Figure 3. **Purified SMALP-encapsulated rhodopsin retains bleaching and regeneration capacity. (a)** Detergent-free, immunoaffinity purification of rhodopsin using the 1D4 mAb. L, soluble ROS (16 ml, 10 µl loaded); FT, flow-through (16 ml, 10 µl loaded); W, wash (15 ml, 10 µl loaded); Elu, elution (1 ml, 10 µl loaded). **(b)** Absorption spectra of purified rhodopsin in SMALPs. Rhodopsin extracted and purified in SMA retains the chromophore throughout purification in the dark (red). Rhodopsin is able to be bleached when exposed to bright light and hydroxylamine and then regenerated by addition of 9-cis-retinal. The regenerated rhodopsin sample retains the chromophore over several days at RT.

higher in the rhodopsin samples (Fig. 4, c and d). Cholesterol levels were found to be higher in rhodopsin samples when compared with the PRPH2/ROM1 samples, while cholesterol ester(18:2) was relatively enriched in the PRPH2/ROM1 samples relative to the rhodopsin samples (Fig. 4 e).

The common phospholipids also displayed multiple significant differences between the rim region and the center (Table 1), especially between PC and PE. There were many differences at the species level within each phospholipid class as well (Fig. 5). There were some instances of differences in PE species between the samples of the two rim proteins, where rhodopsin and PRPH2/ROM1 were relatively higher in PE(16:0_22:6) and PE(18:2_22:6) when compared with ABCA4 (Fig. 5 a). There were also significant differences among individual species in the phosphatidylinositol and PS classes (Fig. 5, b and c). Here, though, the rim samples had similar profiles and were both distinct from rhodopsin samples, further confirming the similarity between the rim sample membranes.

We further evaluated the aggregate relationship between each sample using the unbiased method of principal component analysis (PCA; Fig. 6). PCA produced linear combinations of the 199 separate species across all 14 lipid classes of the initial headgroup data (ROS: n = 2; rhodopsin: n = 3; ABCA4: n = 3; PRPH2/ROM1: n = 3). This global analysis confirmed the general similarity between the rim samples, whereas the center region samples localized to a distinct region of the PCA plot. PC1–3 explained a combined 77.7% of the variance in the system, with PC1 accounting for >46%. When comparing PC1 and PC2, there was obvious clustering of ABCA4 and PRPH2/ROM1 samples along PC1, far removed from rhodopsin on the PC1 axis (Fig. 6 a). The same was true in a comparison of PC1–3 in an all-versus-all 3D plot (Fig. 6 b). The rhodopsin samples grouped tightly and associated more closely with the starting ROS samples with respect to PC1. Analysis of the PCA loadings suggested that PC1 found strongest differences in species across classes containing palmitic and stearic acid (16:0 and 18:0, respectively; corresponding to the rim samples) and chain lengths of 20 or more containing 4–6 unsaturated bonds (rhodopsin samples; Fig. 6 d). We conclude that the lipid compositions of the rim and center regions of ROS disks are distinct at the lipid species level.

Comparisons between the central and rim regions of ROS disks show differences in FA composition

The PCA results suggested that FA chain length and/or unsaturation of the lipids residing in these two functionally distinct areas may be a key differentiator between their membranes. To address this fully, we performed lipid extractions from a new set of SMALP-protein samples (ROS: n = 3; rhodopsin: n = 5; ABCA4: n = 4; PRPH2/ROM1: n = 3), then hydrolyzed the head groups of all lipid species in each sample, followed by FA lipidomic analysis via liquid chromatography–mass spectrometry (LC/MS). The FA compositions of the lipids isolated from the two rim region proteins ABCA4 and PRPH2/ROM1 showed no statistically significant differences in relative molar percent for all chain lengths and saturations. There was considerable difference, however, in the FA composition of the rhodopsin-containing samples when compared with the rim proteins. The rim region proteins copurified with predominantly unsaturated and short chain length FAs, especially 16:0 and 18:0 (Fig. 7 a). Those two FA species accounted for >67% of the full FA content of the ABCA4 sample and >82% of the PRPH2/ROM1 sample. Conversely, the rhodopsin samples contained <30% of these two FAs.

DHA (22:6) is known to be essential to ROS disk health, facilitating rhodopsin activity (Bush et al., 1991; Organisciak et al., 1996; Litman et al., 2001). We found DHA was significantly higher in the central region than in the rim, with a DHA relative molar percentage of 13.5% for rhodopsin samples (Fig. 7 b). The rhodopsin samples were enriched in LC-PUFAs more generally as well, whereas the rim samples contained only 1.6% or less molar percent LC-PUFAs.

Rhodopsin SMALPs also contained more VLC-PUFAs than those in the disk rim (Fig. 7 c). The most prominent VLC-PUFAs found in rhodopsin samples were dotriacontapentaenoic, dotriacontahexaenoic, tetratriacontapentaenoic, and tetratriacontahexaenoic acids (32:5, 32:6, 34:5, and 34:6, respectively), with relative abundances between 0.6% and 1.3%. In contrast, the rim protein SMALPs were sparsely populated with VLC-PUFAs, accounting for 0.2% or less of their total FA content.

Discussion

The first question to be answered by this study is whether lipids that copurify in SMALPs containing purified membrane proteins faithfully represent the native membrane regions from which they are purified. There have been reports that SMALPs composed of pure phospholipids of different types (e.g., PC versus PE) rapidly exchange when incubated together at ambient temperatures, suggesting that native tissues, left solubilizing in SMA for 1–2 h at those temperatures, would result in an

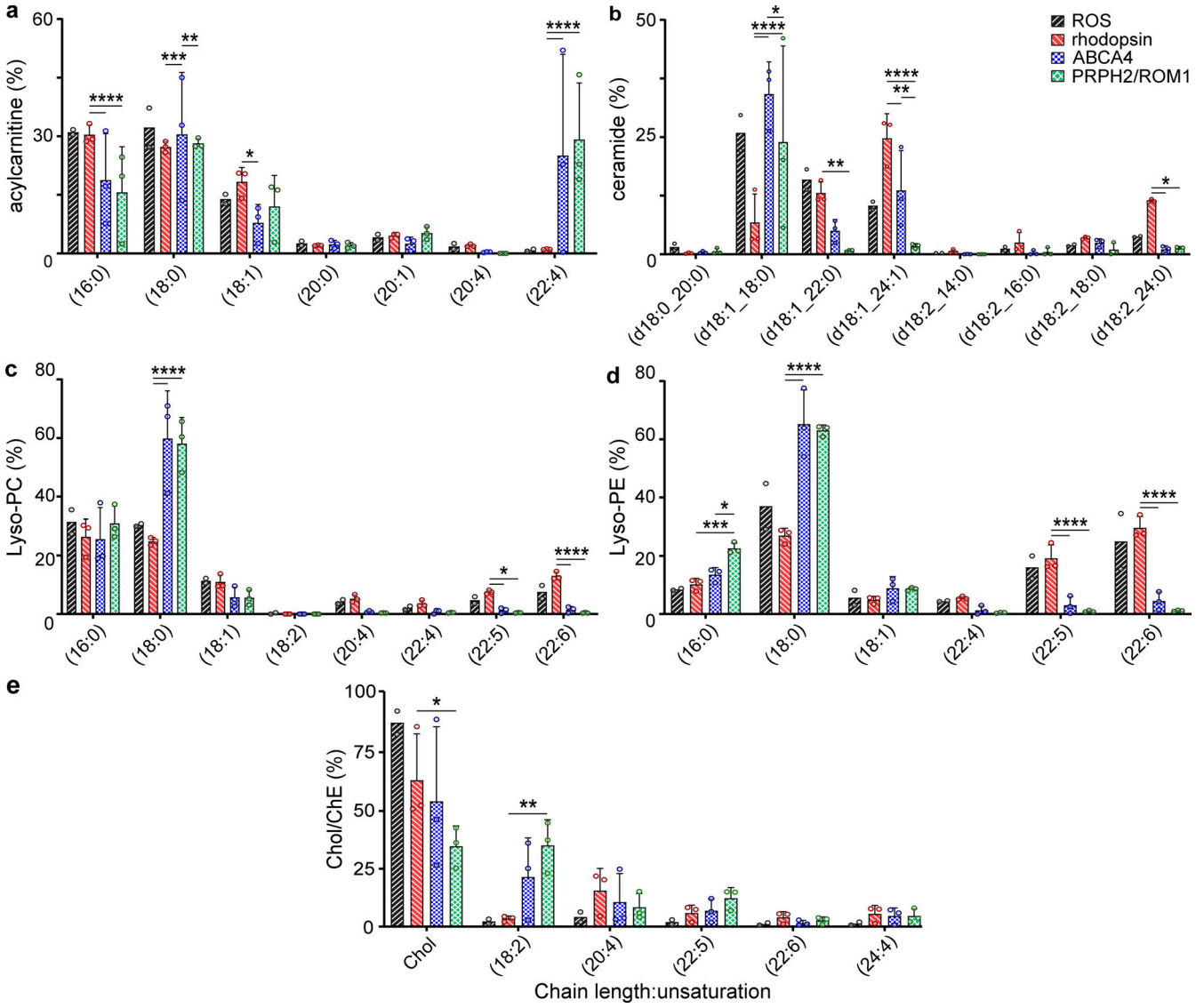

Figure 4. **Lipid compositions of SMALP-embedded ROS membrane proteins are particular to their native location in the membrane. (a–e)** Percentages are shown of every detected species of AcCa, Cer, LPC, LPE, and cholesterol (Chol)/cholesterol ester (ChE), respectively, extracted from SMALPs. Selected species are graphed (all species are shown in Figs. S2, S3, S4, and S5). Total ROS: black forward stripe; rhodopsin: red backward stripe; ABCA4: blue checker; PRPH2/ROM1: green diamond. ROS measured in duplicate as noted by individual data points (open circles). Percent composition was derived from each sample by dividing the area under the curve for each species in a class by the total area under the curve for the class reported via LC/MS after correction for variations in internal standard area, sample mass, and sample injection volume. Statistics were determined using two-way ANOVA with Tukey's multiple comparisons post hoc test. Significance values are indicated as follows: *, P < 0.05; **, P < 0.01; ***, P < 0.001; ****, P < 0.0001.

equilibrated distribution of membrane components among the protein-containing SMALPs (Cuevas Arenas et al., 2017; Schmidt and Sturgis, 2018; Danielczak and Keller, 2018). Prior work on single-target proteins purified in SMALPs from membranes showed little difference between the mother membrane and the extracted, copurifying lipids (Dörr et al., 2014). A recent report on bacterial membrane proteins that associate with the membrane in three distinct ways showed that each purified protein copurified with distinct lipid profiles (Teo et al., 2019). Here, we document definitive differences between samples isolated from different regions of the same mammalian membrane tissue.

The most likely explanation for the preservation of differences between samples is that our purification is performed ≤4°C, which is far below the vast majority of lipid species' main phase melting temperatures. To our knowledge, purification of proteins from native membranes using SMA at this temperature has only been done in one other study, and it reported differences in many species across phospholipid classes (Teo et al., 2019). With the addition of our findings, there remain no reports of lipid transfer in SMALP-protein nanodiscs. While we certainly affirm what was observed in purified bacterial membrane proteins, we provide further evidence that the lipid domains of continuous membranes are distinguishable with SMALPs by the purification and lipidomic analysis of two independent proteins from the same rim region, ABCA4 and PRPH2/ROM1, allowing comparison of their lipid profiles with that of rhodopsin.

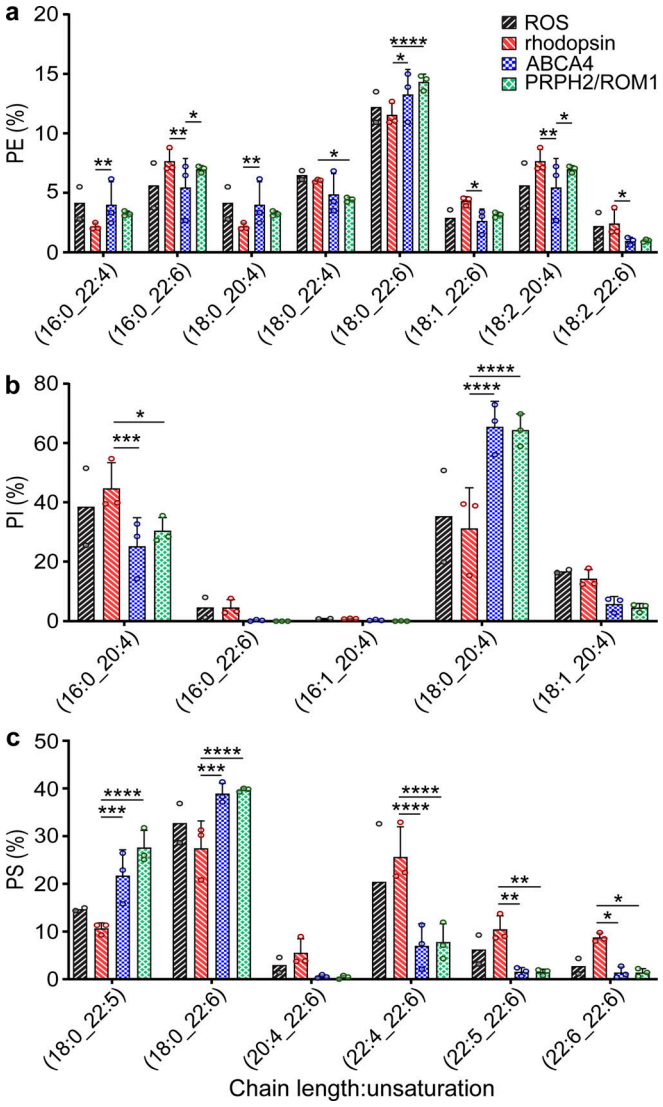

Figure 5. **Phospholipid compositions of SMALP-embedded ROS membrane proteins are particular to their native location in the membrane. (a–c)** Percentages are shown of every detected species of PE, phosphatidylinositol (PI), and PS, extracted from SMALPs; selected phospholipid species are shown here (all phospholipid species are shown in Figs. S2, S3, S4, and S5). Total ROS: black forward stripe; rhodopsin: red backward stripe; ABCA4: blue checker; PRPH2/ROM1: green diamond. ROS measured in duplicate as noted by individual data points (open circles). Major differences are evident between ABCA4 and PRPH2/ROM1 (rim) and rhodopsin (center). Percent composition was derived for each sample by dividing the area under curve for each species in a class by the total area under curve for the class reported via LC/MS after internal standard, sample mass, and sample injection volume correction. The significance of observed differences was determined using two-way ANOVA with Tukey's multiple comparisons post hoc test. Statistical significance values are indicated as follows: *, P < 0.05; **, P < 0.01; ***, P < 0.001; ****, P < 0.0001.

We hypothesized that if the local lipid environment is preserved in SMALPs, then samples of the rim region proteins should show similar lipid profiles to one another, distinct from that of rhodopsin. Our FA chain length/unsaturation analysis revealed no statistically significant differences between the two rim region samples, while clear differences were found between the FA arrays of the rhodopsin and rim protein samples. Furthermore, the cases of statistically significant differences between each rim sample and rhodopsin were nearly identical across all FA chain lengths and saturation levels. Therefore, this study demonstrates that SMA-extracted protein samples from native tissue retain the local environment from which they were isolated.

We approximated the amount of the ROS disk membrane accounted for by the SMALPs of our three chosen samples to assess the completeness of our analysis. We began with the fact that each SMALP will have a certain number of lipids copurifying with it. When ROS membranes are incubated with SMA, ~12-nm-diameter disks of lipids encapsulate bilayer patches of the ROS, with each side of the bilayer representing roughly 113 nm^2 (equaling 226 nm^2 for the full surface area of each native nanodisc; Fig. 1 a). Because of the high density of proteins in the ROS disk membranes, we assumed protein-free SMALP-solubilized membranes would be negligible in amount. Then, with the ROS membrane separated into membrane protein–SMALPs, we estimate the number of lipids that can be accommodated within the SMALP in the presence of each of the known ROS membrane proteins, based the number of transmembrane helices that would occupy a portion of the total SMALP area (T_n). This is done using twice the average cross-sectional area of a transmembrane helix (1.4 nm^2) to account for the helix displacing lipids in both bilayers (Eskandari et al., 1998; Swainsbury et al., 2014; Takamori et al., 2006). The transmembrane helix surface area is then subtracted from the total surface area of the nanodisc membrane to yield the available surface area for lipids within the SMALP. That surface area, divided by the average cross-sectional area of a single phospholipid (~0.78 nm^2), gives the number of lipids that should fit in the given ROS protein SMALP (Lee, 2003). The number of lipids that each membrane protein–SMALP can carry was then scaled by each protein's relative abundance in the ROS membranes. The relative abundance, A_n, was calculated by cross-referencing the nine membrane proteins classified as ROS disk–specific with the ROS disk proteomics reported using absolute protein expression (APEX) measurements taken by tandem mass spectrometry (MS/MS; Skiba et al., 2013; Kwok et al., 2008). This is the estimation of what we call the weighted lipid contribution (WLC) of each protein (Eq. 1).

$$\mathrm{WLC}_n = \mathrm{A}_n \times \frac{[226\mathrm{nm}^2 - (T_n \times 2.8\mathrm{nm}^2)]}{0.78\mathrm{nm}^2}. \quad (1)$$

$\mathrm{WLC}_{\mathrm{rhodopsin}}$, $\mathrm{WLC}_{\mathrm{ABCA4}}$, and $\mathrm{WLC}_{\mathrm{PRPH2/ROM1}}$ were added together and divided by the sum of all WLCs, giving an approximate lipid contribution of 95% from the three samples studied here (Eq. 2 and Table 2).

$$\mathrm{WLC}_{\mathrm{rho,ABCA4,PRPH2/ROM1}} = \frac{\mathrm{WLC}_{\mathrm{rhodopsin}} + \mathrm{WLC}_{\mathrm{ABCA4}} + \mathrm{WLC}_{\mathrm{PRPH2/ROM1}}}{\sum_n \mathrm{WLC}_n}. \quad (2)$$

This estimation gives us confidence that we have studied the majority of the ROS disk membranes.

The stark contrast in the profiles of FA chain lengths between the rim and center of the disks is remarkable (Fig. 7). The center

Table 1. **Comparison of relative phospholipid compositions in native ROS membrane domains[a]**

Phospholipid	Rhodopsin	ABCA4	PRPH2/ROM1	ROS disk[b]	ROS PM[b]
	Copurifying in SMALPs			Isolated in ricin/gold separation	
PC	39.6 ± 3.8	60.9 ± 15.6	60.1 ± 11.8	45.3 ± 3.2	65.1 ± 3.8
PE	54.0 ± 2.7	34.7 ± 17.3	37.0 ± 11.4	41.6 ± 2.6	10.6 ± 2.8
PG	0.2 ± 0.1	0.1 ± 0.1	0.1 ± 0.03	-	-
PI	1.1 ± 0.6	0.6 ± 0.7	0.2 ± 0.1	2.5 ± 0.8	<1.0
PS	5.1 ± 3.4	3.7 ± 2.9	2.6 ± 0.6	13.7 ± 2.1	24.1 ± 2.8

PI, phosphatidylinositol.
[a]Total values for all phospholipids detected in positive mode of LC/MS were used to estimate the relative phospholipid composition in each SMALP-extracted membrane region. Each value is presented as a mean percentage ± SD.
[b]Comparison values from prior ROS disk and PM isolations are taken from Boesze-Battaglia and Albert (1992). Values for PG not included in Boesze-Battaglia and Albert (1992) are noted with "-," and "< 1.0" refers to a value not reported for being <1%.

of the disk is enriched with LC- and VLC-PUFAs relative to the disk rim. The relative abundance of DHA coincident with rhodopsin is consistent with the well-documented requirement of DHA for healthy rhodopsin activity (Mitchell et al., 1992). The relative abundance of eicosatetraenoyl acid (arachidonic acid, 20:4) in the disk center is consistent with its well-known role as a critical precursor for LC- and VLC-PUFAs (Grogan and Lam, 1982; Grogan and Huth, 1983; Grogan, 1984).

On a more general scale, the rhodopsin samples showed that combined VLC-PUFAs represent >15% of total FAs in the center of bovine ROS disks, roughly equivalent to the 13% of whole bovine ROS reported previously (the classification of VLC-PUFA as ≥24 carbons long; Aveldaño and Sprecher, 1987). A particularly intriguing finding was the distinct lack of VLC-PUFAs in the rim region. We had surmised that the slightly wider and curving rim region might provide more space for the extended acyl chains of VLC-PUFAs, but we now deduce that the rim region membranes require the stiffness provided by the abundant 16:0 and 18:0 saturated chains found there.

We were struck by the panoply of components extracted by SMALPs and measured by the lipidomic analysis of the ROS. Many membrane components copurified with the sample proteins, including lyso-PLs, sterols, sphingolipids, AcCas, FFAs, cardiolipin, and mono/di/triglycerides. This comprehensive report (Figs. 4, 5, S2, S3, S4, and S5) of the components of the ROS disk membranes is, to our knowledge, the most complete of any tissue extracted by native nanodiscs. The results of our PCA confirm, in an unbiased manner, that many of the diverse components found in this study are spread anisometrically across the continuous ROS disk membrane, favoring either the center or rim region (Fig. 6). Some of this systematic heterogeneity is likely critical to the maintenance of phototransduction and should be probed more deeply. These data also beg the question of how the asymmetry is initiated and maintained by ROS membrane proteins.

When compared with the prior disk lipidomic analyses, each of the purified SMALPs in our study showed relatively less PS (Table 1; Boesze-Battaglia and Albert, 1992). This may be due to the nature of each study's samples, theirs being total ROS disks and our closest comparison being purified SMALP-rhodopsin. Another possibility is that their method of detection and components detected differed from ours. They quantified the phosphate of HPLC-separated general lipid classes and omitted phosphatidylglycerol, while we compared the phospholipidss detected in positive mode of LC/MS to estimate the relative phospholipid composition. Our method was an estimation based on the sum of many smaller species measurements, while theirs was at the class level to begin with and confirmed each species with TLC. The true proportion of the ROS disk PSs is likely between the two values, but generally will fall between the proportion of phosphatidylinositol and PC/PE, as is the case in both studies.

Differences in content of acyl-carnitine and lyso-PLs are the most notable in the analysis of the lipid classes. While carnitine has been reported to be in ocular tissues, our data further localize at least some of the acyl-carnitine to the center of the ROS disks (Fig. 4 a; Pessotto et al., 1994). Previous work has shown that injection of carnitine in the eye can be protective in a methylcellulose-induced ocular hypertension model, as measured by decreased levels of inducible nitrogen oxide synthase, malondialdehyde, and ubiquitin (Calandrella et al., 2010). Our results, which place AcCa in the immediate vicinity of rhodopsin in the membrane, suggest that carnitine may act as a check on normal oxidative stress in the outer segment (OS) disk membranes. Supplemental carnitine could increase the protective effect afforded the retina by endogenous levels of carnitine in the OS disks, but more evidence is needed to confirm this.

The presence of lyso-PLs has been reported at the tissue level in bovine and human retinas, but their specific function(s) in the retina are yet to be determined (Berdeaux et al., 2010). As a surfactant, LPC has been shown to increase membrane fluidity, which is itself important for protein reorganization in OS disks (Henriksen et al., 2010; Rakshit et al., 2017). Our data show unequivocal differentiation of the lyso-PLs, with short, saturated species in the rim and LC-PUFAs in the center (Fig. 4, c and d). Lyso-PLs consisting of LC-PUFAs likely contribute even more fluidity to the center of the disk. In addition to this general effect, it is conceivable that the lyso-PLs in the center of ROS disks interact specifically with the membrane proteins in a signaling capacity. Lyso-PLs have been shown to interact with GPCRs to initiate $G_{12/13}$, $G_{q/11}$, G_i, and G_s signaling, thereby affecting

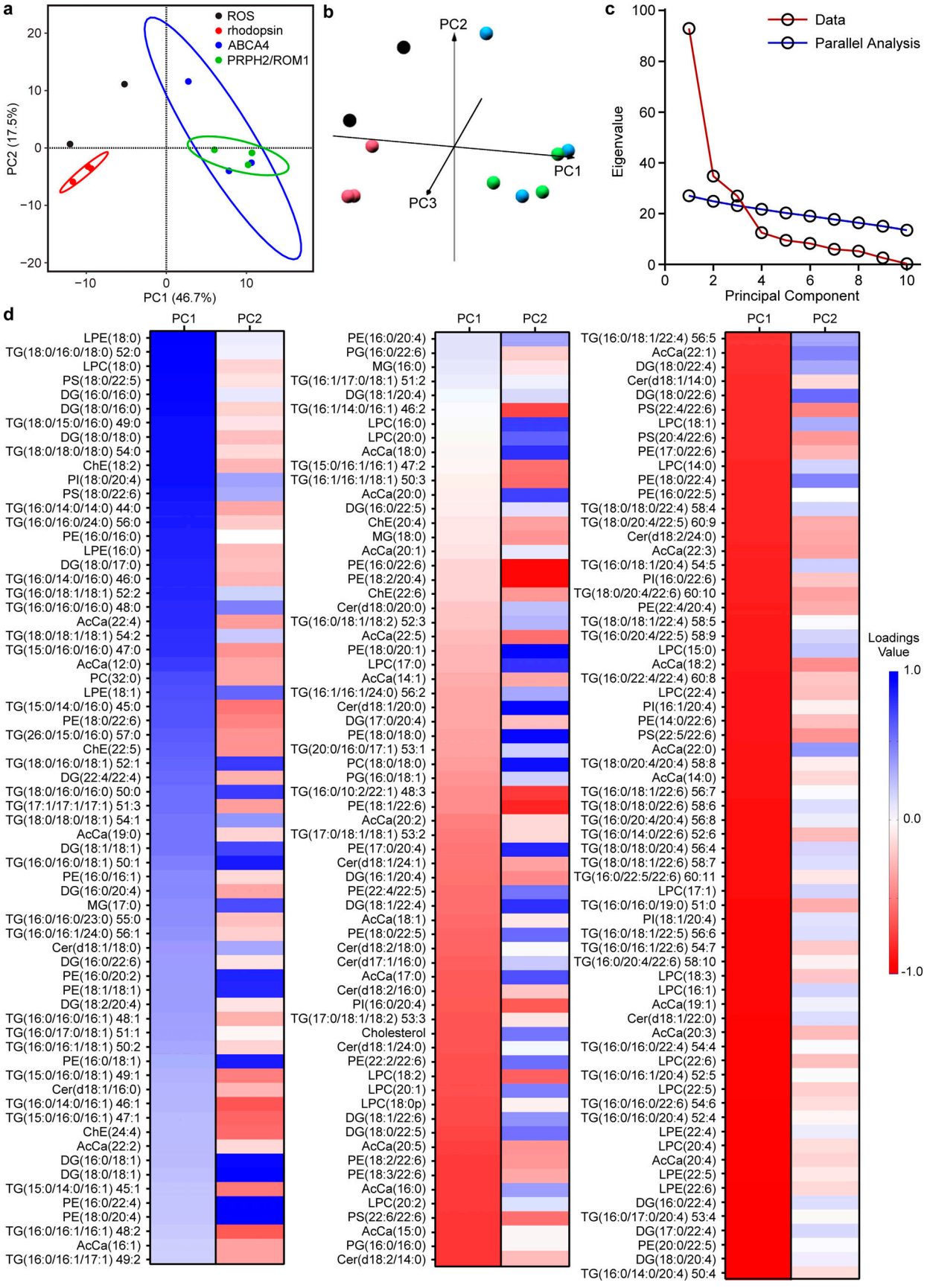

Figure 6. **PCA groups rim region samples apart from central, rhodopsin samples. (a)** PCA of 199 lipid species from 14 lipid classes shows clustering of rim samples away from rhodopsin samples, highlighting, in an unbiased manner, the similarity of the rim membrane lipids and the center region lipids. PC1 and PC2

combined to equal 64.2% of the total variance. **(b)** All-versus-all plot of PC1-3, all of which were found to give higher eigenvalues for the experimental data than the 95th percentile of those made in parallel analysis. **(c)** PC1-3 had eigenvalues >95th percentile of eigenvalues randomly generated through parallel analysis (1,000 simulations conducted). **(d)** Heat plots of loadings used in PCA, sorted by PC1 value, show clear separation based on length/saturation of the lipid species.

various downstream, intracellular signaling pathways (Anliker and Chun, 2004; Xiang et al., 2013; Torkhovskaya et al., 2007; Li et al., 2016). Additional work has shown that light activation of bovine ROS leads to phospholipase A_2 activation, which ties lyso-PL production to light-dependent pathways initiated by rhodopsin signaling (Jelsema, 1987). Rhodopsin is already known to be affected by the membrane composition when transitioning between the Meta I and Meta II states (Gibson and Brown, 1991a, 1991b, 1993; Botelho et al., 2002), but more research is needed to probe the possibility of alternative G protein interactions with rhodopsin for the propagation of lyso-PL signals.

The trend indicating enrichment of free cholesterol toward the center of the disks was surprising as prior data suggested that an exchange of disk cholesterol with the PM causes a gradient of cholesterol from high (nascent disks) to low (mature disks; Boesze-Battaglia et al., 1989). Therefore, we had expected to see a relative increase in free cholesterol in the rim of the disk. One way to explain our result is that the rim, with its highly curved structure, cannot maintain high levels of cholesterol. There may be a separate route for cholesterol movement between disks that allows for the diminution of free cholesterol in maturing disks, but this is only speculation. Regardless, all samples isolated from the disks showed lower relative levels of free cholesterol than the ROS starting material, which contained both disks and PM.

This study, to our knowledge, is the first to extract and purify mammalian membrane proteins along with their corresponding native membrane environment. We were able to document the precise, species-level differences between the two lipid domains of ROS disks (Fig. 8). Our results could provide more context for prior work done on detergent-resistant membranes (DRMs) of the ROS, where Triton X-100–resistant membranes low in rhodopsin and seemingly high in ABCA4 were isolated from the rest of the ROS disks (Martin et al., 2005). The DRMs were shown to have some of the same trends between DRM and fully solubilized regions as seen between the rim and center regions in this work.

Further work should be dedicated to studying physiological protein–lipid interactions of the retina, as many of the key proteins in the visual cycle and phototransduction are membrane proteins. To this end, the process of studying differential membrane composition based on native protein isolation in SMALPs should be expanded to other systems in the hope of uncovering detailed information on the preferred lipid environment of other membrane proteins. In particular, the use of high-resolution lipidomics may help explain pathologies involving critical protein–lipid interactions.

Materials and methods

Animals

All animal protocols were approved by the Institutional Animal Care and Use Committee at the University of California, Irvine, and were conducted in accordance with the Association for Research in Vision and Ophthalmology "Statement for the Use of Animals in Ophthalmical and Visual Research." WT and *Abca4*$^{-/-}$*Rdh8*$^{-/-}$ mice on a BALB/cJ background were used in this study. All mice were housed in the University Laboratory Animal Resources facilities at the University of California, Irvine, and maintained in a 12-h/12-h light-dark cycle environment, and fed Teklad global soy protein-free extruded rodent diet (Envigo) chow and water ad libitum.

Production of mAb CL2 to optimize ABCA4 purification

The C-terminal region of ABCA4 is an accessible site that contains a high-affinity binding epitope for the Rim3F4 antibody. To develop a novel epitope near this site on the C terminus, a 26–amino acid peptide (NETYDLPLHPRTAGASRQAKEVDKGC) from the near-extreme end of bovine ABCA4, with the addition of a C-terminal cysteine, was synthesized and conjugated to keyhole limpet hemocyanin protein to induce an immunogenic response in mice (the procedure was performed by a Genescript antibody production service). CL2 showed lower signal in immunoblots of solubilized bovine ROS in comparison to Rim3F4 and TMR4. Dot blot analysis of the polypeptide used to generate CL2 was conducted to determine whether the epitope was different from that for Rim3F4. Various cleavage products of the polypeptide, purchased from Genescript and designed by sequentially omitting two amino acids from each end, were adsorbed onto the membrane to be probed for CL2 binding. Compared with the full-length peptide, none of the putative subepitopes bound CL2 with nearly the same affinity. When the first residues were removed (ΔF2-6), there was a complete loss of binding, suggesting that they are integral to CL2 recognition. The affinities of those peptides missing the last few residues (ΔL2-6) were much weaker than that of the full-length sequence, indicating that both ends of the epitope are important for robust binding of CL2, differentiating CL2 from Rim3F4.

Extraction of ROS proteins in SMA compared with LMNG solubilization

SMA (2.3:1 styrene:maleic acid ratio; XIRAN SL30010 P20; Polyscope Polymers B.V.) or detergent (LMNG; Anatrace) was incubated at varying concentrations (varied as shown in Fig. S1, a and b, where 2% LMNG was compared with 0.0, 0.5, 1.0, and 2.5% SMA) for 1 h with ROS (isolated as described previously) obtained from three or four bovine retinas in 1 ml of extraction buffer (20 mM bis-tris propane [BTP], pH 7.9, 10% glycerol, 300 mM NaCl, and 1 mM tris[2-carboxyethyl)phosphine] [TCEP]; Papermaster, 1982). The incubations with SMA were conducted at RT, and with detergent at 4°C. All samples were centrifuged at 100,000 *g* for 1 h, and the soluble fractions were separated. Each pellet was resuspended in 10% SDS-containing wash buffer. 10 µl were loaded for each sample

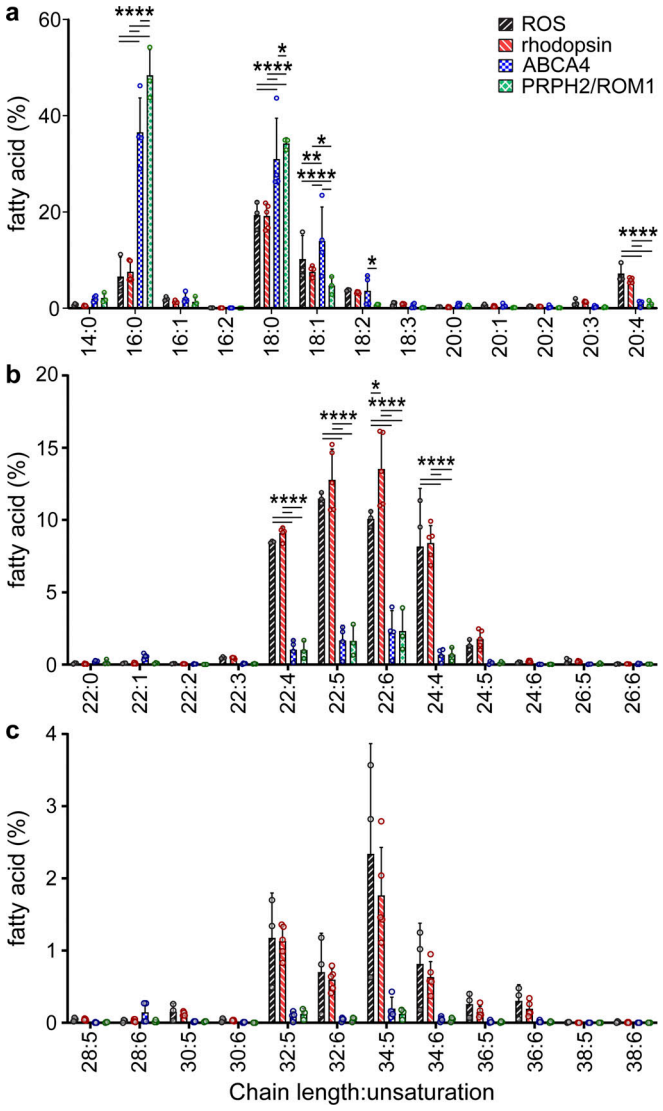

Figure 7. **Comparison of FA chain lengths between the center and rim of ROS disks shows relative enrichment of shorter chain lengths in the rim and LC- and VLC-PUFAs in the center. (a)** Relative molar percentages are shown for every detected class of FA molecule (C14-20) extracted from the SMALPs of each purified protein. **(b)** Relative molar percentages are shown for every detected class of FA molecule (C22-26) extracted from the SMALPs of each purified protein. **(c)** Relative molar percentages are shown for every detected class of FA molecule (C28-38) extracted from the SMALPs of each purified protein. Total ROS: black forward stripe; rhodopsin: red backward stripe; ABCA4: blue checker; PRPH2/ROM1: green diamond. The significance of differences between the means was determined using two-way ANOVA with Tukey's multiple comparisons post hoc test. ROS: $n = 3$, rhodopsin: $n = 5$, ABCA4: $n = 4$, PRPH2/ROM1: $n = 3$. Significance values are indicated as follows: *, $P < 0.05$; **, $P < 0.01$; ****, $P < 0.0001$.

onto a Mini-PROTEAN TGX precast gel, 4–20% gradient (Bio-Rad), and in the case of immunoblot analysis, proteins were transferred to a polyvinylidene difluoride (PVDF) membrane. After blocking for 1 h in 5% (wt/vol) nonfat dry milk, anti-ABCA4 primary antibody TMR4 was added at 1:1,000 dilution from a 1 mg/ml stock, and incubated with the membrane overnight at 4°C. Membranes were washed with PBS containing 0.1% (vol/vol) Tween 20 (PBST), and then anti-mouse IgG (H&L) alkaline phosphatase-conjugated secondary antibody (Promega) was incubated with the membrane at a 1:5,000 dilution for 1 h at RT. After the membranes were again washed with PBST, the blots were developed with Western Blue Stabilized Substrate for Alkaline Phosphatase (Promega) for roughly 15 s, then quenched with ultrapure water.

Immunoblotting of bovine ABCA4 to compare anti-ABCA4 antibodies

ROS from 50 bovine retinas were isolated as described previously and suspended in extraction buffer (20 mM BTP, pH 7.9, 10% glycerol, 300 mM NaCl, and 1 mM TCEP) containing 2% LMNG (Anatrace; Papermaster, 1982). The soluble fraction was separated from insoluble material by centrifugation at 100,000 *g* for 1 h at 4°C. A 10-µl aliquot of the soluble fraction was loaded into each lane of a Mini-PROTEAN TGX precast gel, 4–20% gradient (Bio-Rad), and then proteins were transferred to PVDF membranes. After blocking for 1 h in 5% (wt/vol) nonfat dry milk, primary antibodies against ABCA4, namely CL2, Rim3F4, and TMR4 (Zhang et al., 2015), were added at dilutions of 1:10,000 from 1 mg/ml stocks, and incubated overnight at 4°C. Membranes were washed with PBST, and then anti-mouse IgG (H&L) alkaline phosphatase-conjugated secondary antibodies (Promega) were incubated with the blots at a dilution of 1:5,000 for 1 h at RT. After washing with PBST, blots were developed with Western Blue Stabilized Substrate for Alkaline Phosphatase (Promega) and imaged using an Odyssey Fc imager (LI-COR), using the 700-nm channel with a 2-min exposure time.

Immunoblot of murine retinas to compare anti-ABCA4 antibodies

Murine samples were obtained from the enucleated eyes of WT and *Abca4*$^{-/-}$*Rdh8*$^{-/-}$ mice according to a previously published protocol (Wei et al., 2016). Protein concentrations were determined with a BCA Assay kit (Bio-Rad), following the manufacturer's instructions. Protein samples were mixed with NuPAGE LDS sample buffer and NuPAGE reducing agent, separated using NuPAGE 4–12% Bis-Tris gels (Invitrogen), and transferred to PVDF membranes. Membranes were blocked with 5% (wt/vol) nonfat dry milk and incubated with the CL2 antibody overnight at 4°C. After washing with PBST, membranes were incubated with peroxidase-linked anti-mouse or anti-rabbit IgG (1:10,000; Jackson ImmunoResearch Laboratories) for 1 h at RT. Protein bands were visualized after exposure to SuperSignal West Pico Chemiluminescent substrate (Thermo Fisher Scientific).

Immunohistochemistry of retinal sections to compare anti-ABCA4 antibodies

Mouse eye cups were fixed for 1 h in PBS containing 4% (wt/vol) paraformaldehyde (Sigma-Aldrich) at RT. After fixation, the eye cups were incubated sequentially in PBS containing 10, 20, or 30% (wt/vol) sucrose (Sigma-Aldrich) for 30 min at RT. Then, the eye cups were infiltrated with a 2:1 mixture of PBS containing 30% sucrose and optimal cutting temperature compound (VWR International) and frozen with dry ice. Retinal sections were cut at a thickness of 12 µm and stored at −80°C until use. The retinal sections were rehydrated with PBS and blocked with

Table 2. **Comparison of WLC of ROS disk-specific membrane proteins**

Disk protein	APEX[a]	A_n	T_n	# lipids per protein	WLC	WLC (%)
Rhodopsin	0.1580841	0.663	7	264.6	175.3	68.3
PRPH2/ROM1	0.0614938	0.258	16	232.3	59.9	23.3
ABCA4	0.0073837	0.031	12	246.7	7.6	3.0
GC-1	0.0073970	0.031	1	286.2	8.9	3.5
R9AP	0.0016516	0.007	1	286.2	2.0	0.8
ATP8A2	0.0013005	0.005	10	253.8	1.4	0.5
GC-2	0.0012608	0.005	1	286.2	1.5	0.6

A_n is the APEX value of each protein, n, divided by the sum of all APEX values of disk-specific proteins. T_n is the number of transmembrane helices of each disk-specific protein, n. WLC is the calculated weighted lipid composition of the theoretical SMALP for each protein, as described by Eq. 1. GC-1 and -2 are guanylyl cyclase 1 and 2, respectively. R9AP is regulator of G protein signaling 9-binding protein. ATP8A2 is ATPase aminophospholipid transporter type 8A, member 2. Based on the estimation of WLC percent in the last column, rhodopsin, PRPH2/ROM1, and ABCA4 SMALPs account for 95% of the membrane lipids of ROS disks when extracted in SMA.
[a]Absolute protein expression (APEX) levels are taken from Kwok et al. (2008).

PBS containing 5% (vol/vol) goat serum (Thermo Fisher Scientific) and 0.1% (vol/vol) Triton X-100 (Sigma-Aldrich). After blocking, the sections were incubated with the appropriate primary antibodies diluted in PBS containing 5% goat serum overnight at 4°C. Primary antibodies used for immunohistochemistry were Rim3F4, TMR4, and CL2. The retinal sections were washed with PBS three times for 5 min each and then incubated with Alexa Fluor 488–conjugated goat anti-mouse IgG diluted in PBS containing 5% goat serum at 1:400. After incubation, the retinal sections were washed with PBS three times for 5 min each and then mounted with Vectashield Mounting Medium (Vector Laboratories). The images were acquired with a BZ-X810 Keyence microscope (Keyence) at 20× with numerical aperture of 0.75 at RT with no imaging medium and Alexa Fluor 488 used as the fluorochrome. The camera was built into the BZ-X810 Keyence microscope, and the BZ-X800 viewer from Keyence was the acquisition software. Adobe Photoshop was used to adjust the orientations and Adobe Illustrator to make the figure.

Purification of native, bovine ABCA4 in SMA

Every step of the following purifications was performed in a dark room under dim red light to prevent rhodopsin bleaching-induced aggregation. ROSs and sample-containing fractions were continuously on ice or at 4°C throughout the procedure. ROSs isolated from 50 bovine retinas (isolated as described previously) were extracted in 16 ml of ice-cold extraction buffer with 2.5% SMA (vol/vol; XIRAN SL30010 P20, product received at 1 g/ml; Polyscope Polymers B.V.) for 1 h at 4°C in the dark, followed by centrifugation at 100,000 *g* for 1 h at 4°C (Papermaster, 1982). 1 ml of ∼8.0 mg/ml fresh immunoaffinity resin was prepared by conjugating purified, anti-ABCA4 antibody (CL2) to cyanogen bromide–activated Sepharose 4B beads (GE Healthcare Bio-Sciences) according to the manufacturer's instructions. The extracted fraction of ROS in SMA was then mixed with the immunoaffinity resin, brought to 168 mM NaCl through dilution with SMA wash buffer (20 mM BTP, pH 7.9, 10% glycerol, 35 mM NaCl, and 1 mM TCEP) and incubated for 6 h. The flow-through was collected and used to purify rhodopsin or PRPH2/ROM1. After washing the column with 15 ml of SMA wash buffer, two successive 15-ml washes with high-salt SMA wash buffer (20 mM BTP, pH 7.9, 10% glycerol, 500 mM NaCl, and 1 mM TCEP) were passed over the column, followed by a 15-ml wash with SMA wash buffer. Elution buffer was made by adding 40 mg/ml of CL2 peptide (NETYDLPLHPRTAGASRQAKEVDKGC)

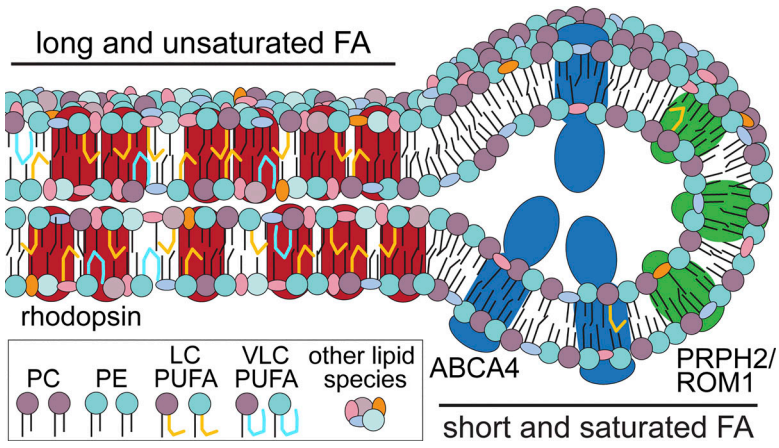

Figure 8. **ROS disks have regionally distinct microenvironments.** The center regions of ROS disks, rich in rhodopsin, have an abundance of long and unsaturated FAs. Rim regions of ROS disks have relatively high amounts of short and saturated FAs. There are many other distinctions in lipid species between the two regions, including relative amounts of PC and PE.

to 1 ml of wash buffer. After the elution step, the column was washed with 1 ml of SMA wash buffer, and then all proteins remaining on the resin were eluted with 1 column volume of 10% SDS. Each lane of the corresponding SDS-PAGE gel represents 10 µl of sample at the concentration of the sample, not adjusted to constant protein concentration across lanes.

Immunoaffinity elution and elution wash fractions of ABCA4 were pooled and concentrated to 0.5 ml and then centrifuged at 20,000 *g* for 10 min. The soluble fraction was then injected onto a Superdex 200 Increase 10/300 GL (GE Healthcare Bio-Sciences) SEC column to remove rhodopsin. SMA SEC buffer (20 mM BTP, pH 7.9, 10 mM NaCl, and 1 mM TCEP) was used as the mobile phase, and 0.5 ml fractions containing ABCA4 were pooled for use in other experiments.

Establishing nanobody (Nb) for PRPH2/ROM1 isolation

Washed ROS membranes from 50 frozen bovine retinas were thawed on ice and resuspended in a detergent-based solubilization buffer (20 mM BTP, pH 7.9, 300 mM NaCl, 2.5 mM DTT, and 25 mM n-dodecyl β-D-maltoside [DDM]) and incubated at 4°C for 1 h with end-over-end mixing. To prevent reactions between free cysteine residues, the crude protein lysate was treated with 5.0 mM iodoacetamide for 30 min at RT. The solution was then quenched with an additional 5 mM DTT and immediately centrifuged at 150,000 *g* for 1 h at 4°C to clear insoluble material and aggregated proteins. The sample was incubated for 1 h at 4°C with end-over-end mixing with Nbs Nb20, Nb19, Nb28, Nb32, and Nb13 to a final ratio of PRPH2/ROM1:Nb of 1:2. 1.0 ml of preequilibrated cOmplete Ni^{2+}-resin (Sigma-Aldrich) was added to the solution and incubated for 1 h at 4°C with end-over-end mixing. The resultant suspension was transferred to a 5.0-ml gravity column. The resin was washed with 10 column volumes of 20 mM BTP, pH 7.9, 300 mM NaCl, 0.35 mM DDM, and 1.0 mM imidazole. Each PRPH2/ROM1/Nb complex was eluted with 4 column volumes elution buffer, comprised of the same wash buffer but with a final imidazole concentration of 300 mM. Aliquots of all samples along the stages of purification were saved for analysis. The resulting eluate was then concentrated, and buffer exchanged to 20 mM BTP, pH 7.9, 300 mM NaCl, and 0.35 mM DDM using a PD-10 column (GE Healthcare Bio-Sciences). The sample was concentrated to 1.0 mg/ml, frozen in liquid nitrogen, and stored at −80°C for future use.

Purification of native, bovine PRPH2/ROM1 in SMA

Starting material for native rhodopsin purification was either the flow-through fraction of the ABCA4 purification, or fresh ROS isolated from 50 bovine retinas, thawed on ice, and resuspended in extraction buffer with 2.5% SMA (vol/vol; XIRAN SL30010 P20; Polyscope Polymers B.V.) and incubated at 4°C for 1 h with end-over-end mixing. To prevent reactions between free cysteine residues, the crude protein lysate was treated with 5.0 mM iodoacetamide for 30 min. The solution was then quenched with an additional 5 mM DTT and immediately centrifuged at 150,000 *g* for 1 h at 4°C to clear insoluble material and aggregated proteins. The sample then was incubated for 1 h at 4°C with end-over-end mixing with PRPH2/ROM1-specific Nb19 to a final ratio of PRPH2/ROM1:Nb19 at 1:2 (Nb19 includes His6 tag). 1.0 ml of preequilibrated cOmplete Ni^{2+}-resin (Sigma-Aldrich) was added to the solution and incubated for 1 h at 4°C with end-over-end mixing. The resultant suspension was transferred to a 5.0-ml gravity column. The resin was washed with 10 column volumes of 20 mM BTP, pH 7.9, 300 mM NaCl, and 1.0 mM imidazole. The PRPH2/ROM1/Nb19 complex was eluted with four column volumes of elution buffer, comprised of the same wash buffer but with a final imidazole concentration of 300 mM. Aliquots of all samples along the stages of the purification were saved for analysis. The resulting elution was then concentrated, and buffer exchanged into 20 mM BTP, pH 7.9, and 300 mM NaCl using a PD-10 column (GE Healthcare). The sample was concentrated to 1.0 mg/ml, frozen in liquid nitrogen, and stored at −80°C for future use.

Purification of native, bovine rhodopsin in SMA

Starting material for native PRPH2/ROM1 purification was either the flow-through fraction of the ABCA4 purification, or fresh ROS isolated from 50 bovine retinas were extracted in 16 ml of ice-cold extraction buffer with 2.5% SMA (vol/vol; XIRAN SL30010 P20; Polyscope Polymers B.V.) for 1 h at 4°C in the dark, followed by centrifugation at 100,000 *g* for 1 h at 4°C. 1 ml of ∼8.0 mg/ml fresh immunoaffinity resin was prepared by conjugating purified anti-rhodopsin antibody (1D4) to cyanogen bromide–activated Sepharose 4B beads (GE Healthcare Bio-Sciences) according to the manufacturer's instructions (Molday and Molday, 2014). The extracted fraction of ROS in SMA was then mixed with the immunoaffinity resin, brought to 168 mM NaCl through dilution with SMA wash buffer (20 mM BTP, pH 7.9, 10% glycerol, 35 mM NaCl, and 1 mM TCEP), and incubated for 6 h. The flow-through was collected and used to purify PRPH2/ROM1. After the column was washed with 15 ml of SMA wash buffer, two successive 15 ml washes with high-salt SMA wash buffer (20 mM BTP, pH 7.9, 10% glycerol, 500 mM NaCl, and 1 mM TCEP) were passed over the column, followed by a 15-ml wash with SMA wash buffer. Elution buffer was made by adding 40 mg/ml of 1D4 peptide (TETSQVAPA) to 1 ml of wash buffer (Molday and Molday, 2014). After the elution step, the column was washed with 1 ml of SMA wash buffer, and then all proteins remaining on the resin were eluted with 1 column volume of 10% SDS. Each lane of the corresponding SDS-PAGE gel represents 10 µl of sample at the concentration of the sample, not adjusted to constant protein concentration across lanes.

Transmission EM

4 µl of the peak SEC fractions containing ABCA4 were adsorbed for 1 min to carbon-coated, glow-discharged grids (15 mA for 15 s; Electron Microscopy Sciences). The grids were washed with two 20-µl drops of ultrapure water and then stained with two 20-µl drops of 1% (wt/vol) uranyl acetate (Electron Microscopy Sciences), the first for 10 s and the second for 1 min. Data were collected with a JEOL JEM-2200fs microscope (JEOL), operated at 200 kV, and equipped with a Tietz TVIPS CCD Camera at 60,000× magnification. The pixel size was 2.131 Å.

Single particle reconstruction

De novo particle reconstruction of SMALP-imbedded ABCA4 was done using the program cisTEM following a published

workflow (Grant et al., 2018). cisTEM auto-picked 71,088 particles that were then sorted by 2D classification into good classes containing 14,652 particles. The particles contained in these classes were then used for cisTEM's ab initio 3D structure generation, which was then refined using cisTEM's Auto Refine. Further structural analysis of ABCA4 was done in UCSF Chimera (Pettersen et al., 2004).

Trp fluorescence quenching assay

All measurements were performed on a PerkinElmer Life Sciences LS55 model fluorometer (PerkinElmer). Binding of ATP to purified ABCA4 in SMALPs was evaluated by monitoring the quenching of protein fluorescence at increasing concentrations of ATP (0–1.5 mM). With the excitation wavelength set at 290 nm, emission spectra were recorded at 330 nm over 1 min with 2-s intervals with bandwidths for excitation and emission fixed at 10 nm. Titrations were performed at 20°C in 20 mM BTP buffer, pH 7.9, containing 35 mM NaCl and 1 mM TCEP. ATP stock solution was diluted in ultrapure water. All binding data were corrected for background and self-absorption of excitation and emission light using a Varian Cary 50 Bio UV-Visible Spectrophotometer.

Rhodopsin absorption assay

All measurements were performed on a Varian Cary 50 Bio UV-Visible Spectrophotometer. Rhodopsin purified in the dark in SMALPs was measured by absorption from 250 to 600 nm. The sample was then incubated with hydroxylamine to a final concentration of 8 mM and allowed to bleach completely in light for 7 min, after which the absorption spectrum was taken. The sample was regenerated with 9-cis-retinal added to a final concentration of 70 µM and allowed to regenerate over 20 min, overnight, and for 2 d, with the spectrum taken at each time point.

Lipid extraction and untargeted lipidomics

Lipids were extracted using a modified version of the Bligh–Dyer method (Bligh and Dyer, 1959). Briefly, samples were shaken in a glass vial (VWR) with 1 ml PBS, 1 ml methanol, and 2 ml chloroform containing internal standards ($^{13}C_{16}$ palmitic acid and $^{2}H_{7}$ cholesterol) for 30 s. The resulting mixture was vortexed for 15 s and centrifuged at 2,400 *g* for 6 min to achieve phase separation. The organic (bottom) layer was retrieved using a Pasteur pipette, dried under a gentle stream of nitrogen, and reconstituted in 2:1 chloroform:methanol for LC/MS analysis.

Lipidomic analysis was performed on a Vanquish HPLC online with a Q-Exactive quadrupole-orbitrap mass spectrometer equipped with an electrospray ion source (Thermo Fisher Scientific). Data were acquired in positive and negative ionization modes. Solvent A consisted of 95:5 water:methanol, Solvent B was 70:25:5 isopropanol:methanol:water. For positive mode, solvents A and B contained 5 mM ammonium formate with 0.1% formic acid; for negative mode, solvents contained 0.028% ammonium hydroxide. An XBridge (Waters) C8 column (5 µm, 4.6 mm × 50 mm) was used. The gradient was held at 0% B between 0 and 5 min, raised to 20% B at 5.1 min, increased linearly from 20 to 100% B between 5.1 and 55 min, held at 100% B between 55 min and 63 min, returned to 0% B at 63.1 min, and held at 0% B until 70 min. Flow rate was 0.1 ml/min from 0 to 5 min, 0.3 ml/min between 5.1 min and 55 min, and 0.4 ml/min between 55 min and 70 min. Spray voltage was 3.5 kV and 2.5 kV for positive and negative ionization modes, respectively; S-lens radio frequency level was 65. Sheath, auxiliary, and sweep gases were 50, 10 and 1 unit(s), respectively. Capillary temperature was 325°C, and auxiliary gas heater temperature was 200°C. Data were collected in full MS/data dependent–MS2 (top 10). Full MS was acquired from 150 to 1,500 m/z with resolution of 70,000, an automatic gain control target of 10^6, and a maximum injection time of 100 ms. MS2 was acquired with resolution of 17,500, a fixed first mass of 50 m/z, an AGC target of 10^5, and a maximum injection time of 200 ms. Stepped normalized collision energies were 20, 30, and 40%.

Lipid extraction and FA lipidomic analysis

For lipid hydrolysis, extracted lipids were resuspended in 200 µl of ethanol and incubated with 0.1 M KOH at RT for 24 h for saponification. The reaction was stopped by addition of 0.2 M HCl. Lipids were extracted as described above with $^{2}H_{31}$ palmitic acid as an internal standard.

FA lipidomic analysis was performed on a Dionex Ultimate 3000 LC system (Thermo Fisher Scientific) coupled to a TSQ Quantiva mass spectrometer (Thermo Fisher Scientific). Solvent A consisted of 95:5 water:methanol. Solvent B was 70:25:5 isopropanol:methanol:water. For negative mode, solvents contained 0.028% ammonium hydroxide. An XBridge C8 column (5 µm, 4.6 mm × 50 mm; Waters) was used. The gradient was as described in the section "Lipid extraction and untargeted lipidomics." MS analyses were performed using electrospray ionization in negative ion mode, with spay voltages of −2.5 kV, ion transfer tube temperature of 325°C, and vaporizer temperature of 200°C. Sheath, auxiliary, and sweep gases were 40, 10, and 1, respectively. Pseudo-multiple reaction monitoring was performed for all FAs.

Lipid data analysis

Lipid identification was performed with LipidSearch (Thermo Fisher Scientific). Mass accuracy, chromatography, and peak integration of all LipidSearch-identified lipids and targeted lipids were verified with Skyline (MacLean et al., 2010). Peak areas were used in data reporting, and data were normalized using internal standards. Quantification of the FFAs was performed by measuring the area under the peak, and the "raw" value is reported as relative molar percentage of total area under the curve for each sample. In cases of two peaks for a single species (e.g., the result of omega-3 versus omega-6 differences in FA), we added the peak areas together and reported the species without omega-3/6 differentiation. Each lipid class was then normalized separately such that the sum of all species of a class equaled 100%. These relative molar percentages were used for all graphs and analyses. In cases of fewer than three samples for a particular species, the species was excluded from all ANOVA analysis. All lipid species found across all samples were used for PCA (199 total species, 14 classes). PCA scores, loadings, and variances were calculated using Graphpad Prism software

(Graphpad). Principal components 1, 2, and 3 (PC1, PC2, and PC3, respectively) were included in our analysis because they passed Horn's parallel analysis test (1,000 iterations; Horn, 1965). For two-way ANOVA measurements throughout, data distribution was assumed to be normal, but was not formally tested.

Online supplemental material

Fig. S1 shows SMA extraction of ROS, characterization of anti-ABCA4 mAb CL2 with murine and bovine samples, and nsTEM analysis of ABCA4 purified with CL2 in SMA shows increased TMD density. Figs. S2, S3, S4, and S5 show the full list of lipid species detected, with each species amount graphed as the percent of the total for each particular class (PC, PE, etc.).

Acknowledgments

We thank David Peck, Tim Dinh, and Dr. Huajun Yan for isolation of the bovine retinas. We also thank Dr. Brian Kevany for help with the initial nanobody expression and screening. The XIRAN-series SMA was provided by Polyscope Polymers B.V. The CL2 antibody was continuously produced by Denice Major at the Visual Science Research Core of Case Western Reserve University (Cleveland, OH), supported by P30 EY11373.

This research was supported in part by grants to K. Palczewski from the National Institutes of Health (NIH; EY009339, EY027283, EY030873, and EY019312); and to P.D. Kiser from the U.S. Department of Veterans Affairs (I01BX004939). D. Skowronska-Krawczyk was supported by a grant from the Thome Memorial Foundation Program in Age-Related Macular Degeneration Research. C.L. Sander was supported by National Eye Institute–funded predoctoral fellowships T32EY007157-17 and T32EY007157-16A1. E.H. Choi was supported by predoctoral fellowships T32GM007250 and T32GM008803. S. Suh was supported by predoctoral fellowships F30EY029136-01A1, T32EY024236, and T32GM007250. The authors also acknowledge support from a Research to Prevent Blindness unrestricted grant to the Department of Ophthalmology, University of California, Irvine. This work was also supported by the Mass Spectrometry Core of the Salk Institute with funding from NIH-National Cancer Institute Cancer Center Support Grant (P30 014195) and the Helmsley Center for Genomic Medicine. The MS data described here were gathered on a Thermo Fisher Q Exactive Hybrid Quadrupole Orbitrap mass spectrometer funded by National Institutes of Health grant 1S10OD021815-01. Molecular graphics and analyses were performed with UCSF Chimera, developed by the Resource for Biocomputing, Visualization, and Informatics at the University of California, San Francisco, with support from National Institutes of Health grant P41-GM103311.

C.L. Sander, H. Jin, and K. Palczewski have filed for a patent on the CL2 mAb; they declare no additional competing financial interests. The other authors declare no competing financial interests.

Author contributions: C.L. Sander helped design the antigen for the CL2 mAb; designed, performed, and/or analyzed the results of all experiments; and wrote and revised the manuscript. A.E. Sears developed the Nb19 nanobody and the purification of PRPH2/ROM1 and helped write and revise the manuscript. A.F.M. Pinto and A. Saghatelian helped design and carried out the lipidomic data collection and performed initial data analysis. E.H. Choi performed immunohistochemistry of murine and bovine ROS samples and revised the manuscript. S. Kahremany helped design and perform rhodopsin regeneration experiments and revised the manuscript. F. Gao performed FA analysis of materials in revision. D. Salom helped characterize the ROS membranes. S. Suh performed immunoblots of murine samples and revised the manuscript. H. Jin helped design the antigen for the CL2 mAb and revised the manuscript. E. Pardon and J. Steyaert developed and provided the original Nb families for screening against PRPH2/ROM1 and helped edit the manuscript. Z. Dong provided mouse retina cryosections. D. Skowronska-Krawczyk helped design the lipidomic experiments and revised the manuscript. P.D. Kiser helped design all experiments and revised the manuscript. K. Palczewski helped design the antigen for the CL2 mAb, helped design all experiments, and revised the manuscript.

Submitted: 11 January 2021
Revised: 26 April 2021
Accepted: 18 May 2021

References

Agbaga, M.-P., R.S. Brush, M.N.A. Mandal, K. Henry, M.H. Elliott, and R.E. Anderson. 2008. Role of Stargardt-3 macular dystrophy protein (ELOVL4) in the biosynthesis of very long chain fatty acids. *Proc. Natl. Acad. Sci. USA.* 105:12843–12848. https://doi.org/10.1073/pnas.0802607105

Agbaga, M.-P., M.N.A. Mandal, and R.E. Anderson. 2010. Retinal very long-chain PUFAs: new insights from studies on ELOVL4 protein. *J. Lipid Res.* 51:1624–1642. https://doi.org/10.1194/jlr.R005025

Ahn, J., J.T. Wong, and R.S. Molday. 2000. The effect of lipid environment and retinoids on the ATPase activity of ABCR, the photoreceptor ABC transporter responsible for Stargardt macular dystrophy. *J. Biol. Chem.* 275:20399–20405. https://doi.org/10.1074/jbc.M000555200

Albert, A.D., J.E. Young, and Z. Paw. 1998. Phospholipid fatty acyl spatial distribution in bovine rod outer segment disk membranes. *Biochim. Biophys. Acta.* 1368:52–60. https://doi.org/10.1016/S0005-2736(97)00200-9

Anliker, B., and J. Chun. 2004. Lysophospholipid G protein-coupled receptors. *J. Biol. Chem.* 279:20555–20558. https://doi.org/10.1074/jbc.R400013200

Aveldaño, M.I. 1988. Phospholipid species containing long and very long polyenoic fatty acids remain with rhodopsin after hexane extraction of photoreceptor membranes. *Biochemistry.* 27:1229–1239. https://doi.org/10.1021/bi00404a024

Aveldaño, M.I., and H. Sprecher. 1987. Very long chain (C24 to C36) polyenoic fatty acids of the n-3 and n-6 series in dipolyunsaturated phosphatidylcholines from bovine retina. *J. Biol. Chem.* 262:1180–1186. https://doi.org/10.1016/S0021-9258(19)75768-8

Bada Juarez, J.F., J.C. Muñoz-García, R. Inácio dos Reis, A. Henry, D. McMillan, M. Kriek, M. Wood, C. Vandenplas, Z. Sands, L. Castro, et al. 1862. 2020. Detergent-free extraction of a functional low-expressing GPCR from a human cell line. *Biochim. Biophys. Acta Biomembr.* 183152. https://doi.org/10.1016/j.bbamem.2019.183152

Bennett, L.D., R.S. Brush, M. Chan, T.A. Lydic, K. Reese, G.E. Reid, J.V. Busik, M.H. Elliott, and R.E. Anderson. 2014. Effect of reduced retinal VLC-PUFA on rod and cone photoreceptors. *Invest. Ophthalmol. Vis. Sci.* 55:3150–3157. https://doi.org/10.1167/iovs.14-13995

Berdeaux, O., P. Juaneda, L. Martine, S. Cabaret, L. Bretillon, and N. Acar. 2010. Identification and quantification of phosphatidylcholines containing very-long-chain polyunsaturated fatty acid in bovine and human retina using liquid chromatography/tandem mass spectrometry.

J. Chromatogr. A. 1217:7738–7748. https://doi.org/10.1016/j.chroma.2010.10.039

Bernstein, P.S., J. Tammur, N. Singh, A. Hutchinson, M. Dixon, C.M. Pappas, N.A. Zabriskie, K. Zhang, K. Petrukhin, M. Leppert, and R. Allikmets. 2001. Diverse macular dystrophy phenotype caused by a novel complex mutation in the ELOVL4 gene. *Invest. Ophthalmol. Vis. Sci.* 42:3331–3336.

Bligh, E.G., and W.J. Dyer. 1959. A rapid method of total lipid extraction and purification. *Can. J. Biochem. Physiol.* 37:911–917. https://doi.org/10.1139/o59-099

Boesze-Battaglia, K., and A.D. Albert. 1992. Phospholipid distribution among bovine rod outer segment plasma membrane and disk membranes. *Exp. Eye Res.* 54:821–823. https://doi.org/10.1016/0014-4835(92)90040-Y

Boesze-Battaglia, K., T. Hennessey, and A.D. Albert. 1989. Cholesterol heterogeneity in bovine rod outer segment disk membranes. *J. Biol. Chem.* 264:8151–8155. https://doi.org/10.1016/S0021-9258(18)83162-3

Botelho, A.V., N.J. Gibson, R.L. Thurmond, Y. Wang, and M.F. Brown. 2002. Conformational energetics of rhodopsin modulated by nonlamellar-forming lipids. *Biochemistry.* 41:6354–6368. https://doi.org/10.1021/bi011995g

Bush, R.A., C.E. Remé, and A. Malnoë. 1991. Light damage in the rat retina: the effect of dietary deprivation of N-3 fatty acids on acute structural alterations. *Exp. Eye Res.* 53:741–752. https://doi.org/10.1016/0014-4835(91)90109-R

Calandrella, N., C. De Seta, G. Scarsella, and G. Risuleo. 2010. Carnitine reduces the lipoperoxidative damage of the membrane and apoptosis after induction of cell stress in experimental glaucoma. *Cell Death Dis.* 1:e62. https://doi.org/10.1038/cddis.2010.40

Chen, W., W.J. Esselman, D.B. Jump, and J.V. Busik. 2005. Anti-inflammatory effect of docosahexaenoic acid on cytokine-induced adhesion molecule expression in human retinal vascular endothelial cells. *Invest. Ophthalmol. Vis. Sci.* 46:4342–4347. https://doi.org/10.1167/iovs.05-0601

Chen, W., D.B. Jump, W.J. Esselman, and J.V. Busik. 2007. Inhibition of cytokine signaling in human retinal endothelial cells through modification of caveolae/lipid rafts by docosahexaenoic acid. *Invest. Ophthalmol. Vis. Sci.* 48:18–26. https://doi.org/10.1167/iovs.06-0619

Chen, H., J.A. Tran, A. Eckerd, T.-P. Huynh, M.H. Elliott, R.S. Brush, and N.A. Mandal. 2013. Inhibition of de novo ceramide biosynthesis by FTY720 protects rat retina from light-induced degeneration. *J. Lipid Res.* 54:1616–1629. https://doi.org/10.1194/jlr.M035048

Chen, D., D.L. Chao, L. Rocha, M. Kolar, V.A. Nguyen Huu, M. Krawczyk, M. Dasyani, T. Wang, M. Jafari, M. Jabari, et al. 2020. The lipid elongation enzyme ELOVL2 is a molecular regulator of aging in the retina. *Aging Cell.* 19:e13100. https://doi.org/10.1111/acel.13100

Cuevas Arenas, R., B. Danielczak, A. Martel, L. Porcar, C. Breyton, C. Ebel, and S. Keller. 2017. Fast Collisional Lipid Transfer Among Polymer-Bounded Nanodiscs. *Sci. Rep.* 7:45875. https://doi.org/10.1038/srep45875

Daemen, F.J.M. 1973. Vertebrate rod outer segment membranes. *Biochim. Biophys. Acta.* 300:255–288. https://doi.org/10.1016/0304-4157(73)90006-3

Danielczak, B., and S. Keller. 2018. Collisional lipid exchange among DIBMA-encapsulated nanodiscs (DIBMALPs). *Eur. Polym. J.* 109:206–213. https://doi.org/10.1016/j.eurpolymj.2018.09.043

Dörr, J.M., M.C. Koorengevel, M. Schäfer, A.V. Prokofyev, S. Scheidelaar, E.A.W. van der Cruijsen, T.R. Dafforn, M. Baldus, and J.A. Killian. 2014. Detergent-free isolation, characterization, and functional reconstitution of a tetrameric K+ channel: the power of native nanodiscs. *Proc. Natl. Acad. Sci. USA.* 111:18607–18612. https://doi.org/10.1073/pnas.1416205112

Edwards, A.O., L.A. Donoso, and R. Ritter III. 2001. A novel gene for autosomal dominant Stargardt-like macular dystrophy with homology to the SUR4 protein family. *Invest. Ophthalmol. Vis. Sci.* 42:2652–2663.

Eskandari, S., E.M. Wright, M. Kreman, D.M. Starace, and G.A. Zampighi. 1998. Structural analysis of cloned plasma membrane proteins by freeze-fracture electron microscopy. *Proc. Natl. Acad. Sci. USA.* 95:11235–11240. https://doi.org/10.1073/pnas.95.19.11235

Falk, G., and P. Fatt. 1969. Distinctive properties of the lamellar and disk-edge structures of the rod outer segment. *J. Ultrastruct. Res.* 28:41–60. https://doi.org/10.1016/S0022-5320(69)90005-7

Fung, B.K., J.B. Hurley, and L. Stryer. 1981. Flow of information in the light-triggered cyclic nucleotide cascade of vision. *Proc. Natl. Acad. Sci. USA.* 78:152–156. https://doi.org/10.1073/pnas.78.1.152

Gakhar, S., S.H. Risbud, and M.L. Longo. 2020. Structure retention of silica gel-encapsulated bacteriorhodopsin in purple membrane and in lipid nanodiscs. *Colloids Surf. B Biointerfaces.* 186:110680. https://doi.org/10.1016/j.colsurfb.2019.110680

Ganapathy, S., L. Opdam, Y. Hontani, S. Frehan, Q. Chen, K.J. Hellingwerf, H.J.M. de Groot, J.T.M. Kennis, and W.J. de Grip. 2020. 2020. Membrane matters: The impact of a nanodisc-bilayer or a detergent microenvironment on the properties of two eubacterial rhodopsins. *Biochim. Biophys. Acta Biomembr.* 1862:183113. https://doi.org/10.1016/j.bbamem.2019.183113

Gibson, N.J., and M.F. Brown. 1991a. Role of phosphatidylserine in the MI-MII equilibrium of rhodopsin. *Biochem. Biophys. Res. Commun.* 176:915–921. https://doi.org/10.1016/S0006-291X(05)80273-6

Gibson, N.J., and M.F. Brown. 1991b. Membrane lipid influences on the energetics of the metarhodopsin I and metarhodopsin II conformational states of rhodopsin probed by flash photolysis. *Photochem. Photobiol.* 54:985–992. https://doi.org/10.1111/j.1751-1097.1991.tb02120.x

Gibson, N.J., and M.F. Brown. 1993. Lipid headgroup and acyl chain composition modulate the MI-MII equilibrium of rhodopsin in recombinant membranes. *Biochemistry.* 32:2438–2454. https://doi.org/10.1021/bi00060a040

Giusto, N.M., S.J. Pasquaré, G.A. Salvador, and M.G. Ilincheta de Boschero. 2010. Lipid second messengers and related enzymes in vertebrate rod outer segments. *J. Lipid Res.* 51:685–700. https://doi.org/10.1194/jlr.R001891

Goldberg, A.F.X., and R.S. Molday. 1996a. Subunit composition of the peripherin/rds-rom-1 disk rim complex from rod photoreceptors: hydrodynamic evidence for a tetrameric quaternary structure. *Biochemistry.* 35:6144–6149. https://doi.org/10.1021/bi960259n

Goldberg, A.F.X., and R.S. Molday. 1996b. Defective subunit assembly underlies a digenic form of retinitis pigmentosa linked to mutations in peripherin/rds and rom-1. *Proc. Natl. Acad. Sci. USA.* 93:13726–13730. https://doi.org/10.1073/pnas.93.24.13726

Gorusupudi, A., R. Rallabandi, B. Li, R. Arunkumar, J.D. Blount, G.T. Rognon, F.-Y. Chang, A. Wade, S. Lucas, J.C. Conboy, et al. 2021. Retinal bioavailability and functional effects of a synthetic very-long-chain polyunsaturated fatty acid in mice. *Proc. Natl. Acad. Sci. USA.* 118:e2017739118. https://doi.org/10.1073/pnas.2017739118

Grant, T., A. Rohou, and N. Grigorieff. 2018. *cis*TEM, user-friendly software for single-particle image processing. *eLife.* 7:e35383. https://doi.org/10.7554/eLife.35383

Grogan, W.M. 1984. Metabolism of arachidonate in rat testis: characterization of 26-30 carbon polyenoic acids. *Lipids.* 19:341–346. https://doi.org/10.1007/BF02534785

Grogan, W.M., and E.G. Huth. 1983. Biosynthesis of long-chain polyenoic acids from arachidonic acid in cultures of enriched spermatocytes and spermatids from mouse testis. *Lipids.* 18:275–284. https://doi.org/10.1007/BF02534702

Grogan, W.M., and J.W. Lam. 1982. Fatty acid synthesis in isolated spermatocytes and spermatids of mouse testis. *Lipids.* 17:604–611. https://doi.org/10.1007/BF02535366

Gulati, S., M. Jamshad, T.J. Knowles, K.A. Morrison, R. Downing, N. Cant, R. Collins, J.B. Koenderink, R.C. Ford, M. Overduin, et al. 2014. Detergent-free purification of ABC (ATP-binding-cassette) transporters. *Biochem. J.* 461:269–278. https://doi.org/10.1042/BJ20131477

Hamano, F., H. Kuribayashi, T. Iwagawa, A. Tsuhako, K. Nagata, H. Sagara, T. Shimizu, H. Shindou, and S. Watanabe. 2021. Mapping membrane lipids in the developing and adult mouse retina under physiological and pathological conditions using mass spectrometry. *J. Biol. Chem.* 296:100303. https://doi.org/10.1016/j.jbc.2021.100303

Heck, M., and K.P. Hofmann. 2001. Maximal rate and nucleotide dependence of rhodopsin-catalyzed transducin activation: initial rate analysis based on a double displacement mechanism. *J. Biol. Chem.* 276:10000–10009. https://doi.org/10.1074/jbc.M009475200

Henriksen, J.R., T.L. Andresen, L.N. Feldborg, L. Duelund, and J.H. Ipsen. 2010. Understanding detergent effects on lipid membranes: a model study of lysolipids. *Biophys. J.* 98:2199–2205. https://doi.org/10.1016/j.bpj.2010.01.037

Hiebler, S., T. Masuda, J.G. Hacia, A.B. Moser, P.L. Faust, A. Liu, N. Chowdhury, N. Huang, A. Lauer, J. Bennett, et al. 2014. The Pex1-G844D mouse: a model for mild human Zellweger spectrum disorder. *Mol. Genet. Metab.* 111:522–532. https://doi.org/10.1016/j.ymgme.2014.01.008

Horn, J.L. 1965. A rationale and test for the number of factors in factor analysis. *Psychometrika.* 30:179–185. https://doi.org/10.1007/BF02289447

Hubbard, R., and G. Wald. 1952. Cis-trans isomers of vitamin A and retinene in the rhodopsin system. *J. Gen. Physiol.* 36:269–315. https://doi.org/10.1085/jgp.36.2.269

Illing, M., L.L. Molday, and R.S. Molday. 1997. The 220-kDa rim protein of retinal rod outer segments is a member of the ABC transporter

superfamily. *J. Biol. Chem.* 272:10303–10310. https://doi.org/10.1074/jbc.272.15.10303

Jamshad, M., Y.-P. Lin, T.J. Knowles, R.A. Parslow, C. Harris, M. Wheatley, D.R. Poyner, R.M. Bill, O.R.T. Thomas, M. Overduin, and T.R. Dafforn. 2011. Surfactant-free purification of membrane proteins with intact native membrane environment. *Biochem. Soc. Trans.* 39:813–818. https://doi.org/10.1042/BST0390813

Jamshad, M., J. Charlton, Y.-P. Lin, S.J. Routledge, Z. Bawa, T.J. Knowles, M. Overduin, N. Dekker, T.R. Dafforn, R.M. Bill, et al. 2015. G-protein coupled receptor solubilization and purification for biophysical analysis and functional studies, in the total absence of detergent. *Biosci. Rep.* 35:e00188. https://doi.org/10.1042/BSR20140171

Jelsema, C.L. 1987. Light activation of phospholipase A2 in rod outer segments of bovine retina and its modulation by GTP-binding proteins. *J. Biol. Chem.* 262:163–168. https://doi.org/10.1016/S0021-9258(19)75904-3

Kessler, C., M. Tillman, M.E. Burns, and E.N. Pugh Jr. 2014. Rhodopsin in the rod surface membrane regenerates more rapidly than bulk rhodopsin in the disc membranes in vivo. *J. Physiol.* 592:2785–2797. https://doi.org/10.1113/jphysiol.2014.272518

Kevany, B.M., Y. Tsybovsky, I.D.G. Campuzano, P.D. Schnier, A. Engel, and K. Palczewski. 2013. Structural and functional analysis of the native peripherin-ROM1 complex isolated from photoreceptor cells. *J. Biol. Chem.* 288:36272–36284. https://doi.org/10.1074/jbc.M113.520700

Knowles, T.J., R. Finka, C. Smith, Y.-P. Lin, T. Dafforn, and M. Overduin. 2009. Membrane proteins solubilized intact in lipid containing nanoparticles bounded by styrene maleic acid copolymer. *J. Am. Chem. Soc.* 131:7484–7485. https://doi.org/10.1021/ja810046q

Kwok, M.C.M., J.M. Holopainen, L.L. Molday, L.J. Foster, and R.S. Molday. 2008. Proteomics of photoreceptor outer segments identifies a subset of SNARE and Rab proteins implicated in membrane vesicle trafficking and fusion. *Mol. Cell. Proteomics.* 7:1053–1066. https://doi.org/10.1074/mcp.M700571-MCP200

Lee, A.G. 2003. Lipid–protein interactions in biological membranes: a structural perspective. *Biochim. Biophys. Acta.* 1612:1–40. https://doi.org/10.1016/S0005-2736(03)00056-7

Li, Y.-F., R.-S. Li, S.B. Samuel, R. Cueto, X.-Y. Li, H. Wang, and X.-F. Yang. 2016. Lysophospholipids and their G protein-coupled receptors in atherosclerosis. *Front. Biosci.* 21:70–88. https://doi.org/10.2741/4377

Litman, B.J., S.L. Niu, A. Polozova, and D.C. Mitchell. 2001. The role of docosahexaenoic acid containing phospholipids in modulating G protein-coupled signaling pathways: visual transduction. *J. Mol. Neurosci.* 16: 237–242, discussion:279–284. https://doi.org/10.1385/JMN:16:2-3:237

Liu, A., J. Chang, Y. Lin, Z. Shen, and P.S. Bernstein. 2010. Long-chain and very long-chain polyunsaturated fatty acids in ocular aging and age-related macular degeneration. *J. Lipid Res.* 51:3217–3229. https://doi.org/10.1194/jlr.M007518

Loewen, C.J.R., and R.S. Molday. 2000. Disulfide-mediated oligomerization of Peripherin/Rds and Rom-1 in photoreceptor disk membranes. Implications for photoreceptor outer segment morphogenesis and degeneration. *J. Biol. Chem.* 275:5370–5378. https://doi.org/10.1074/jbc.275.8.5370

Logan, S., and R.E. Anderson. 2014. Dominant Stargardt Macular Dystrophy (STGD3) and ELOVL4. *In* Retinal Degenerative Diseases. J.D. Ash, C. Grimm, J.G. Hollyfield, R.E. Anderson, M.M. LaVail, and C. Bowes Rickman, editors. Springer, New York. 447–453. https://doi.org/10.1007/978-1-4614-3209-8_57

Logan, S., M.-P. Agbaga, M.D. Chan, N. Kabir, N.A. Mandal, R.S. Brush, and R.E. Anderson. 2013. Deciphering mutant ELOVL4 activity in autosomal-dominant Stargardt macular dystrophy. *Proc. Natl. Acad. Sci. USA.* 110:5446–5451. https://doi.org/10.1073/pnas.1217251110

MacLean, B., D.M. Tomazela, N. Shulman, M. Chambers, G.L. Finney, B. Frewen, R. Kern, D.L. Tabb, D.C. Liebler, and M.J. MacCoss. 2010. Skyline: an open source document editor for creating and analyzing targeted proteomics experiments. *Bioinformatics.* 26:966–968. https://doi.org/10.1093/bioinformatics/btq054

Martin, R.E., M.H. Elliott, R.S. Brush, and R.E. Anderson. 2005. Detailed characterization of the lipid composition of detergent-resistant membranes from photoreceptor rod outer segment membranes. *Invest. Ophthalmol. Vis. Sci.* 46:1147–1154. https://doi.org/10.1167/iovs.04-1207

McMahon, A., and W. Kedzierski. 2010. Polyunsaturated very-long-chain C28-C36 fatty acids and retinal physiology. *Br. J. Ophthalmol.* 94: 1127–1132. https://doi.org/10.1136/bjo.2008.149286

Milstein, M.L., B.L. Cavanaugh, N.M. Roussey, S. Volland, D.S. Williams, and A.F.X. Goldberg. 2020. Multistep peripherin-2/rds self-assembly drives membrane curvature for outer segment disk architecture and photoreceptor viability. *Proc. Natl. Acad. Sci. USA.* 117:4400–4410. https://doi.org/10.1073/pnas.1912513117

Mitchell, D.C., M. Straume, J.L. Miller, and B.J. Litman. 1990. Modulation of metarhodopsin formation by cholesterol-induced ordering of bilayer lipids. *Biochemistry.* 29:9143–9149. https://doi.org/10.1021/bi00491a007

Mitchell, D.C., M. Straume, and B.J. Litman. 1992. Role of sn-1-saturated,sn-2-polyunsaturated phospholipids in control of membrane receptor conformational equilibrium: effects of cholesterol and acyl chain unsaturation on the metarhodopsin I in equilibrium with metarhodopsin II equilibrium. *Biochemistry.* 31:662–670. https://doi.org/10.1021/bi00118a005

Molday, L.L., and R.S. Molday. 2014. 1D4: a versatile epitope tag for the purification and characterization of expressed membrane and soluble proteins. *Methods Mol. Biol.* 1177:1–15. https://doi.org/10.1007/978-1-4939-1034-2_1

Molday, R.S., and K. Zhang. 2010. Defective lipid transport and biosynthesis in recessive and dominant Stargardt macular degeneration. *Prog. Lipid Res.* 49:476–492. https://doi.org/10.1016/j.plipres.2010.07.002

Nathans, J. 1992. Rhodopsin: structure, function, and genetics. *Biochemistry.* 31:4923–4931. https://doi.org/10.1021/bi00136a001

Oluwole, A.O., B. Danielczak, A. Meister, J.O. Babalola, C. Vargas, and S. Keller. 2017. Solubilization of Membrane Proteins into Functional Lipid-Bilayer Nanodiscs Using a Diisobutylene/Maleic Acid Copolymer. *Angew. Chem. Int. Ed. Engl.* 56:1919–1924. https://doi.org/10.1002/anie.201610778

Organisciak, D.T., R.M. Darrow, Y.L. Jiang, and J.C. Blanks. 1996. Retinal light damage in rats with altered levels of rod outer segment docosahexaenoate. *Invest. Ophthalmol. Vis. Sci.* 37:2243–2257.

Palczewski, K. 2006. G protein-coupled receptor rhodopsin. *Annu. Rev. Biochem.* 75:743–767. https://doi.org/10.1146/annurev.biochem.75.103004.142743

Papermaster, D.S. 1982. Preparation of retinal rod outer segments. *Methods Enzymol.* 81:48–52. https://doi.org/10.1016/S0076-6879(82)81010-0

Pardon, E., T. Laeremans, S. Triest, S.G.F. Rasmussen, A. Wohlkönig, A. Ruf, S. Muyldermans, W.G.J. Hol, B.K. Kobilka, and J. Steyaert. 2014. A general protocol for the generation of Nanobodies for structural biology. *Nat. Protoc.* 9:674–693. https://doi.org/10.1038/nprot.2014.039

Pessotto, P., P. Valeri, and E. Arrigoni-Martelli. 1994. The presence of L-carnitine in ocular tissues of the rabbit. *J. Ocul. Pharmacol.* 10:643–651. https://doi.org/10.1089/jop.1994.10.643

Pettersen, E.F., T.D. Goddard, C.C. Huang, G.S. Couch, D.M. Greenblatt, E.C. Meng, and T.E. Ferrin. 2004. UCSF Chimera--a visualization system for exploratory research and analysis. *J. Comput. Chem.* 25:1605–1612. https://doi.org/10.1002/jcc.20084

Polans, A., W. Baehr, and K. Palczewski. 1996. Turned on by Ca2+! The physiology and pathology of Ca(2+)-binding proteins in the retina. *Trends Neurosci.* 19:547–554. https://doi.org/10.1016/S0166-2236(96)10059-X

Qian, H., X. Zhao, P. Cao, J. Lei, N. Yan, and X. Gong. 2017. Structure of the Human Lipid Exporter ABCA1. *Cell.* 169:1228–1239.e10. https://doi.org/10.1016/j.cell.2017.05.020

Quazi, F., and R.S. Molday. 2013. Differential phospholipid substrates and directional transport by ATP-binding cassette proteins ABCA1, ABCA7, and ABCA4 and disease-causing mutants. *J. Biol. Chem.* 288:34414–34426. https://doi.org/10.1074/jbc.M113.508812

Quazi, F., S. Lenevich, and R.S. Molday. 2012. ABCA4 is an N-retinylidene-phosphatidylethanolamine and phosphatidylethanolamine importer. *Nat. Commun.* 3:925. https://doi.org/10.1038/ncomms1927

Rakshit, T., S. Senapati, V.M. Parmar, B. Sahu, A. Maeda, and P.S.-H. Park. 2017. Adaptations in rod outer segment disc membranes in response to environmental lighting conditions. *Biochim. Biophys. Acta Mol. Cell Res.* 1864:1691–1702. https://doi.org/10.1016/j.bbamcr.2017.06.013

Rotstein, N.P., and M.I. Aveldaño. 1988. Synthesis of very long chain (up to 36 carbon) tetra, penta and hexaenoic fatty acids in retina. *Biochem. J.* 249: 191–200. https://doi.org/10.1042/bj2490191

Routledge, S.J., M. Jamshad, H.A. Little, Y.-P. Lin, J. Simms, A. Thakker, C.M. Spickett, R.M. Bill, T.R. Dafforn, D.R. Poyner, et al. 2020. 2020. Ligand-induced conformational changes in a SMALP-encapsulated GPCR. *Biochim. Biophys. Acta Biomembr.* 1862:183235. https://doi.org/10.1016/j.bbamem.2020.183235

SanGiovanni, J.P., E.Y. Chew, T.E. Clemons, M.D. Davis, F.L. Ferris III, G.R. Gensler, N. Kurinij, A.S. Lindblad, R.C. Milton, J.M. Seddon, and R.D. Sperduto. Age-Related Eye Disease Study Research Group. 2007. The relationship of dietary lipid intake and age-related macular degeneration in a case-control study: AREDS Report No. 20. *Arch. Ophthalmol.* 125:671–679. https://doi.org/10.1001/archopht.125.5.671

Sapieha, P., A. Stahl, J. Chen, M.R. Seaward, K.L. Willett, N.M. Krah, R.J. Dennison, K.M. Connor, C.M. Aderman, E. Liclican, et al. 2011. 5-Lipoxygenase Metabolite 4-HDHA Is a Mediator of the Antiangiogenic Effect of Ω-3 Polyunsaturated Fatty Acids. *Sci. Transl. Med.* 3:69ra12. https://doi.org/10.1126/scitranslmed.3001571

Schmidt, V., and J.N. Sturgis. 2018. Modifying styrene-maleic acid copolymer for studying lipid nanodiscs. *Biochim. Biophys. Acta Biomembr.* 1860:777–783. https://doi.org/10.1016/j.bbamem.2017.12.012

Seddon, J.M., J. Cote, and B. Rosner. 2003. Progression of age-related macular degeneration: association with dietary fat, transunsaturated fat, nuts, and fish intake. *Arch. Ophthalmol.* 121:1728–1737. https://doi.org/10.1001/archopht.121.12.1728

Seddon, J.M., S. George, and B. Rosner. 2006. Cigarette smoking, fish consumption, omega-3 fatty acid intake, and associations with age-related macular degeneration: the US Twin Study of Age-Related Macular Degeneration. *Arch. Ophthalmol.* 124:995–1001. https://doi.org/10.1001/archopht.124.7.995

Simonelli, F., C. Manna, N. Romano, G. Nunziata, O. Voto, and E. Rinaldi. 1996. Evaluation of fatty acids in membrane phospholipids of erythrocytes in retinitis pigmentosa patients. *Ophthalmic Res.* 28:93–98. https://doi.org/10.1159/000267880

Skiba, N.P., W.J. Spencer, R.Y. Salinas, E.C. Lieu, J.W. Thompson, and V.Y. Arshavsky. 2013. Proteomic identification of unique photoreceptor disc components reveals the presence of PRCD, a protein linked to retinal degeneration. *J. Proteome Res.* 12:3010–3018. https://doi.org/10.1021/pr4003678

Suh, M., A.A. Wierzbicki, and M.T. Clandinin. 1994. Dietary fat alters membrane composition in rod outer segments in normal and diabetic rats: Impact on content of very-long-chain (C > or = 24) polyenoic fatty acids. *Biochim. Biophys. Acta.* 1214:54–62. https://doi.org/10.1016/0005-2760(94)90009-4

Sun, H., and J. Nathans. 2001. Mechanistic studies of ABCR, the ABC transporter in photoreceptor outer segments responsible for autosomal recessive Stargardt disease. *J. Bioenerg. Biomembr.* 33:523–530. https://doi.org/10.1023/A:1012883306823

Swainsbury, D.J.K., S. Scheidelaar, R. van Grondelle, J.A. Killian, and M.R. Jones. 2014. Bacterial reaction centers purified with styrene maleic acid copolymer retain native membrane functional properties and display enhanced stability. *Angew. Chem. Int. Ed. Engl.* 53:11803–11807. https://doi.org/10.1002/anie.201406412

Takamori, S., M. Holt, K. Stenius, E.A. Lemke, M. Grønborg, D. Riedel, H. Urlaub, S. Schenck, B. Brügger, P. Ringler, et al. 2006. Molecular anatomy of a trafficking organelle. *Cell.* 127:831–846. https://doi.org/10.1016/j.cell.2006.10.030

Teo, A.C.K., S.C. Lee, N.L. Pollock, Z. Stroud, S. Hall, A. Thakker, A.R. Pitt, T.R. Dafforn, C.M. Spickett, and D.I. Roper. 2019. Analysis of SMALP co-extracted phospholipids shows distinct membrane environments for three classes of bacterial membrane protein. *Sci. Rep.* 9:1813. https://doi.org/10.1038/s41598-018-37962-0

Tikhonenko, M., T.A. Lydic, Y. Wang, W. Chen, M. Opreanu, A. Sochacki, K.M. McSorley, R.L. Renis, T. Kern, D.B. Jump, et al. 2010. Remodeling of retinal Fatty acids in an animal model of diabetes: a decrease in long-chain polyunsaturated fatty acids is associated with a decrease in fatty acid elongases Elovl2 and Elovl4. *Diabetes.* 59:219–227. https://doi.org/10.2337/db09-0728

Tikhonenko, M., T.A. Lydic, M. Opreanu, S. Li Calzi, S. Bozack, K.M. McSorley, A.L. Sochacki, M.S. Faber, S. Hazra, S. Duclos, et al. 2013. N-3 polyunsaturated Fatty acids prevent diabetic retinopathy by inhibition of retinal vascular damage and enhanced endothelial progenitor cell reparative function. *PLoS One.* 8:e55177. https://doi.org/10.1371/journal.pone.0055177

Torkhovskaya, T.I., O.M. Ipatova, T.S. Zakharova, M.M. Kochetova, and E.M. Khalilov. 2007. Lysophospholipid receptors in cell signaling. *Biochemistry (Mosc.).* 72:125–131. https://doi.org/10.1134/S0006297907020010

Tsybovsky, Y., T. Orban, R.S. Molday, D. Taylor, and K. Palczewski. 2013. Molecular organization and ATP-induced conformational changes of ABCA4, the photoreceptor-specific ABC transporter. *Structure.* 21:854–860. https://doi.org/10.1016/j.str.2013.03.001

Ueta, T., K. Kojima, T. Hino, M. Shibata, S. Nagano, and Y. Sudo. 2020. Applicability of Styrene-Maleic Acid Copolymer for Two Microbial Rhodopsins, RxR and HsSRI. *Biophys. J.* 119:1760–1770. https://doi.org/10.1016/j.bpj.2020.09.026

Wei, H., Z. Xun, H. Granado, A. Wu, and J.T. Handa. 2016. An easy, rapid method to isolate RPE cell protein from the mouse eye. *Exp. Eye Res.* 145:450–455. https://doi.org/10.1016/j.exer.2015.09.015

Xiang, S.Y., S.S. Dusaban, and J.H. Brown. 2013. Lysophospholipid receptor activation of RhoA and lipid signaling pathways. *Biochim. Biophys. Acta.* 1831:213–222. https://doi.org/10.1016/j.bbalip.2012.09.004

Zhang, K., M. Kniazeva, M. Han, W. Li, Z. Yu, Z. Yang, Y. Li, M.L. Metzker, R. Allikmets, D.J. Zack, et al. 2001. A 5-bp deletion in ELOVL4 is associated with two related forms of autosomal dominant macular dystrophy. *Nat. Genet.* 27:89–93. https://doi.org/10.1038/83817

Zhang, N., Y. Tsybovsky, A.V. Kolesnikov, M. Rozanowska, M. Swider, S.B. Schwartz, E.M. Stone, G. Palczewska, A. Maeda, V.J. Kefalov, et al. 2015. Protein misfolding and the pathogenesis of ABCA4-associated retinal degenerations. *Hum. Mol. Genet.* 24:3220–3237. https://doi.org/10.1093/hmg/ddv073

Zimmerman, W.F., and S. Keys. 1989. Lysophospholipase and the metabolism of lysophosphatidylcholine in isolated bovine rod outer segments. *Exp. Eye Res.* 48:69–76. https://doi.org/10.1016/0014-4835(89)90020-1

Zulliger, R., S.M. Conley, M.L. Mwoyosvi, M.R. Al-Ubaidi, and M.I. Naash. 2018. Oligomerization of Prph2 and Rom1 is essential for photoreceptor outer segment formation. *Hum. Mol. Genet.* 27:3507–3518. https://doi.org/10.1093/hmg/ddy240

JCB

Supplemental material

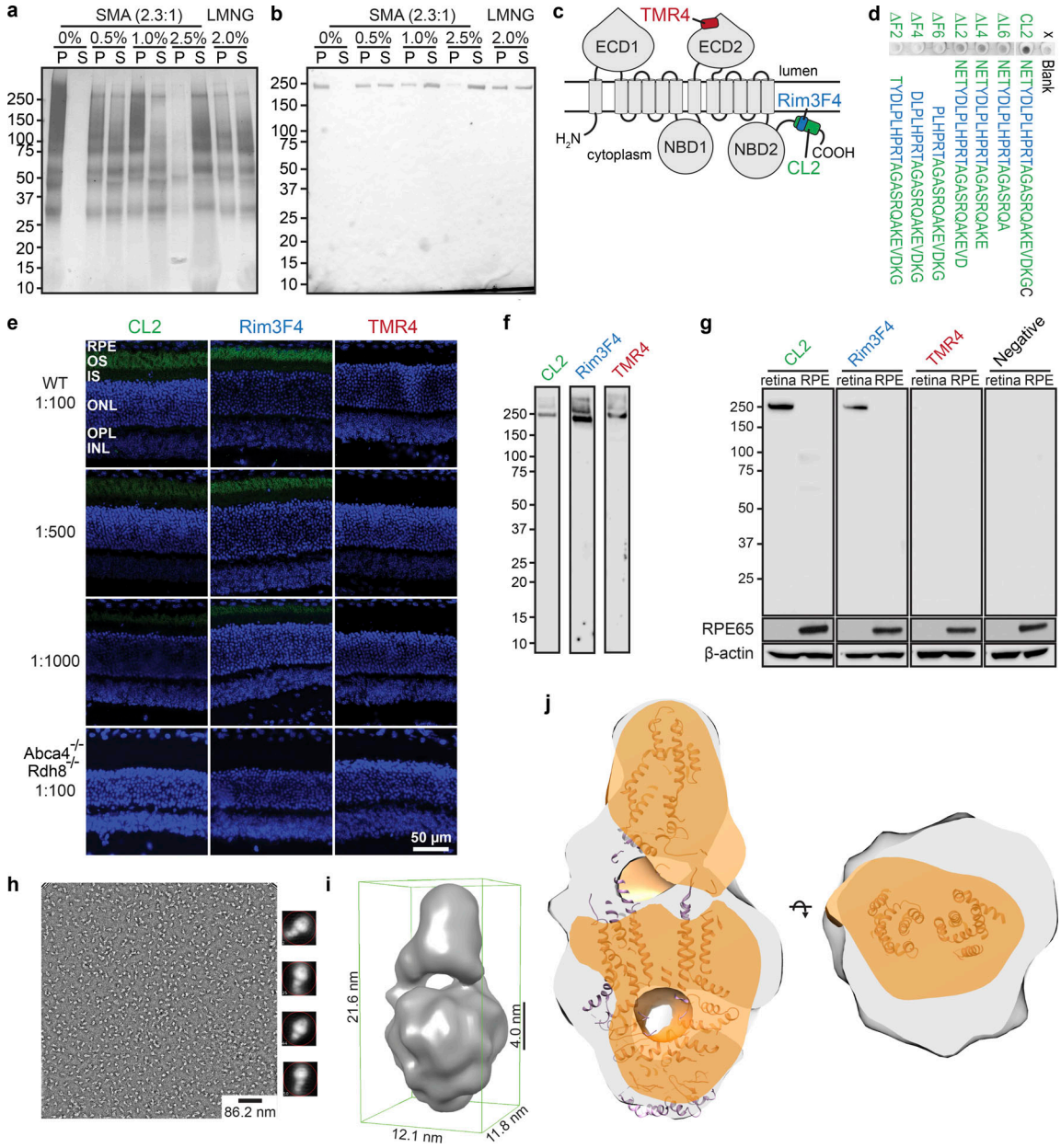

Figure S1. **Interrogation of ABCA4 extracted in SMA and the mAb generated for its immunoaffinity purification, CL2. (a)** SDS-PAGE gel of the extraction of ROS proteins by various concentrations of SMA, or by the low critical micelle concentration detergent LMNG. Residual ROS pellets after initial detergent extraction were solubilized with 10% SDS. P, pellet; S, soluble. **(b)** Immunoblotting demonstrates a graded extraction of ABCA4 with increasing amounts of SMA. **(c)** Topographical map of ABCA4 highlighting the epitopes of three mAbs, TMR4, Rim3F4, and CL2. **(d)** Dot blots of polypeptides comprised of the amino acid chains shown to the right were used to confirm the novel epitope of CL2 on the C terminus of ABCA4. Truncations of the beginning of the sequence decreased the binding of CL2. The Rim3F4 epitope is depicted in blue. **(e)** Immunohistochemistry of retinal cryosections from 2-mo-old WT and *Abca4*$^{-/-}$*Rdh8*$^{-/-}$ knockout (KO) mice, using CL2, Rim3F4, and TMR4 antibodies against ABCA4 (green) at three different dilutions. As expected, no fluorescence signal occurred with the KO mouse cryosections. With cryosections from WT mice, primary incubations with CL2 and Rim3F4 antibodies showed specific immunoreactivity with photoreceptor outer segments at all three dilutions, whereas TMR4 did not generate a fluorescence signal. Scale bar: 50 µm. **(f)** Relative amount of ABCA4 present in solubilized bovine ROS as assessed by immunoblotting. Stock concentrations of 1 mg/ml were used for all antibodies, and the dilution was 1:10,000 for each antibody tested. **(g)** Immunoblot of retinal and retinal pigment epithelium lysates obtained from 2-mo-old WT mouse using CL2, Rim3F4, and TMR4 antibodies. Probing with CL2 and Rim3F4 antibodies resulted in a specific band at 250 kD in the retinal samples, which corresponds to the size of ABCA4, whereas no positive signal was detected with TMR4. Retinal pigment epithelium-specific 65 kDa protein (RPE65) served as the control for tissue sample purity, and β-actin (42 kD) served as the loading control. **(h)** Negative stain micrograph of a representative SMA-CL2 preparation with 2D classes to the right; 60,000× magnification. SMALP-extracted ABCA4 shows an increase in TMD density, indicative of a native lipid belt. Scale bar: 86.2 nm. **(i)** 3D reconstruction of ABCA4 at ∼18 Å resolution showing a putative bilayer thickness in the region of the SMALP. **(j)** SMALP-imbedded ABCA4 (gray) shows considerably more density within the predicted TMD region compared with (1) a prior ABCA4 negative-stained structure (EMDB-5497 [orange], solubilized in DDM and then switched into amphipol); and (2) the ABCA4 homologue, ABCA1 (EMDB-6724 [purple ribbon], solubilized in DDM and cholesterol hemisuccinate and then switched into digitonin). We interpret these differences to be explained by the SMALP nanodisc containing native lipids surrounding the TMD of ABCA4. IS, inner segment; ONL, outer nuclear layer; OPL, outer plexiform layer; INL, inner nuclear layer.

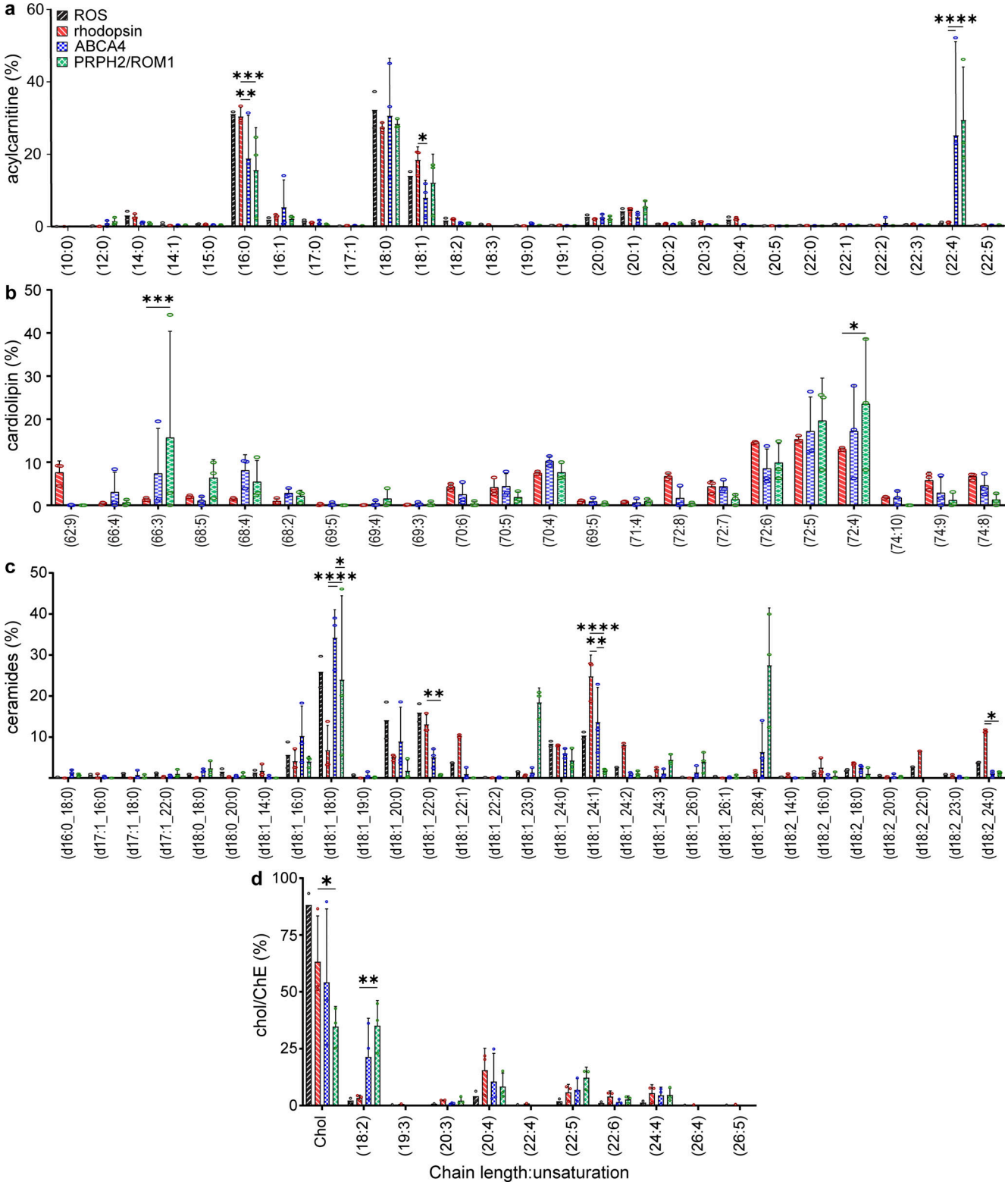

Figure S2. **Complete compositional analysis of detected species for AcCa, cardiolipin, Cer, and cholesterol (chol)/cholesterol ester (ChE). (a–d)** Every detected species of lipid that copurified with each sample is shown as a percentage of each respective class (class noted on y axis). Cardiolipin chain lengths and unsaturation levels are summed together. Total ROS: black forward stripe; rhodopsin: red backward stripe; ABCA4: blue checker; PRPH2/ROM1: green diamond. The number of measurements for each sample of each species varies, as noted by the individual data points for each bar (open circles). Percent composition was calculated for each sample by dividing the area under the curve for each species in a class by the total area under the curve for that class, measured via LC/MS after correction for variations in internal standard area, sample mass, and sample injection volume. Statistics were determined using two-way ANOVA with Tukey's multiple comparisons post hoc test between samples that had at least three detected replicates. Statistical significance values are indicated as follows: *, $P < 0.05$; **, $P < 0.01$; ***, $P < 0.001$; ****, $P < 0.0001$.

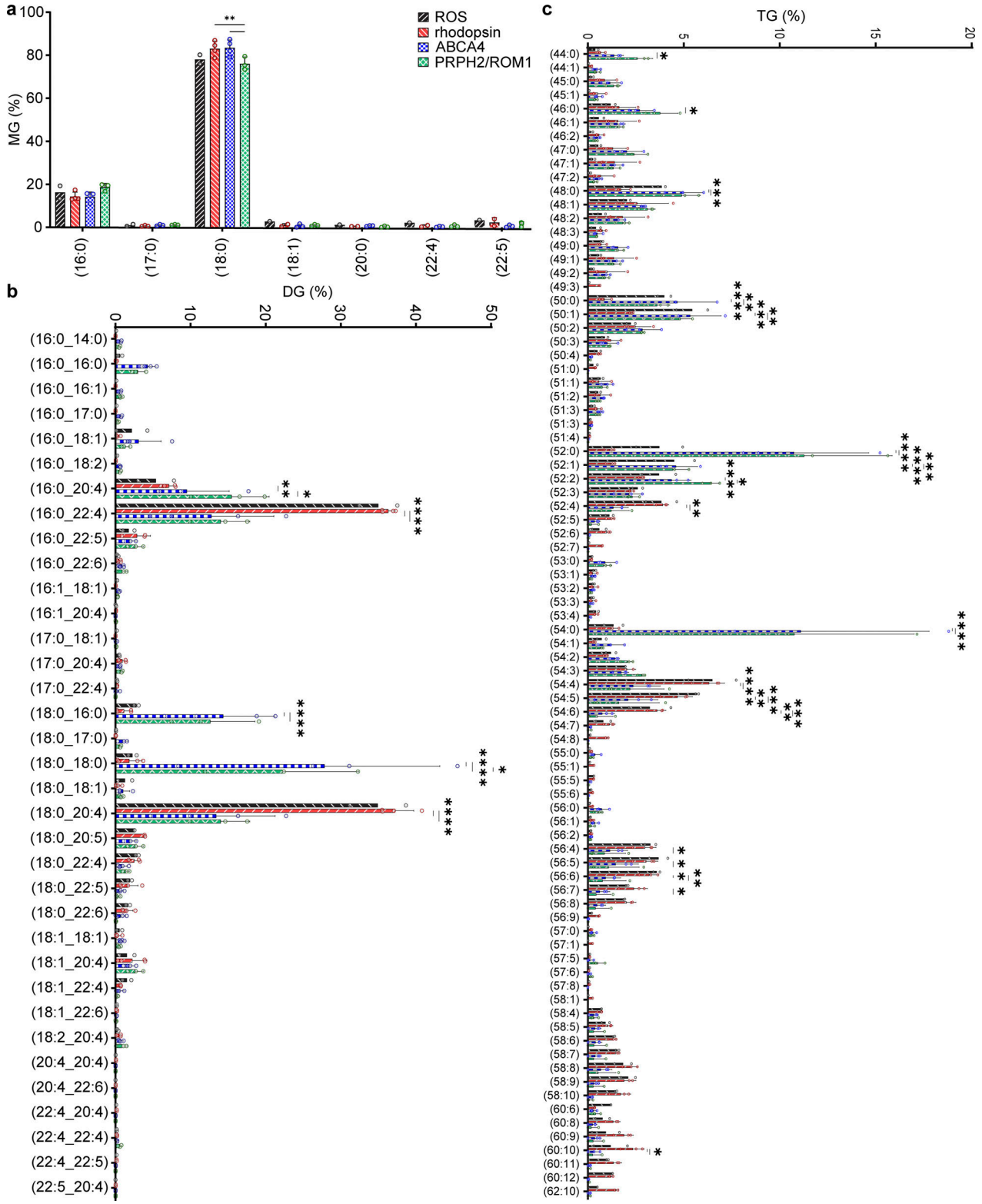

Figure S3. **Complete compositional analysis of detected species for mono- (MG), di- (DG), and triacylglicerides (TG). (a–c)** Every detected species of lipid that copurified with each sample is shown as a percentage of each respective class (class noted on y axis). Triacylgliceride chain lengths and unsaturation levels summed together. Total ROS: black forward stripe; rhodopsin: red backward stripe; ABCA4: blue checker; PRPH2/ROM1: green diamond. The number of measurements for each sample of each species varies, as noted by the individual data points for each bar. Percent composition was calculated for each sample by dividing the area under the curve for each species in a class by the total area under the curve for that class, measured via LC/MS after correction for variations in internal standard area, sample mass, and sample injection volume. Statistics are determined using two-way ANOVA with Tukey's multiple comparisons post hoc test between samples that had at least three detected replicates. Statistical significance values are indicated as follows: *, $P < 0.05$; **, $P < 0.01$; ***, $P < 0.001$; ****, $P < 0.0001$.

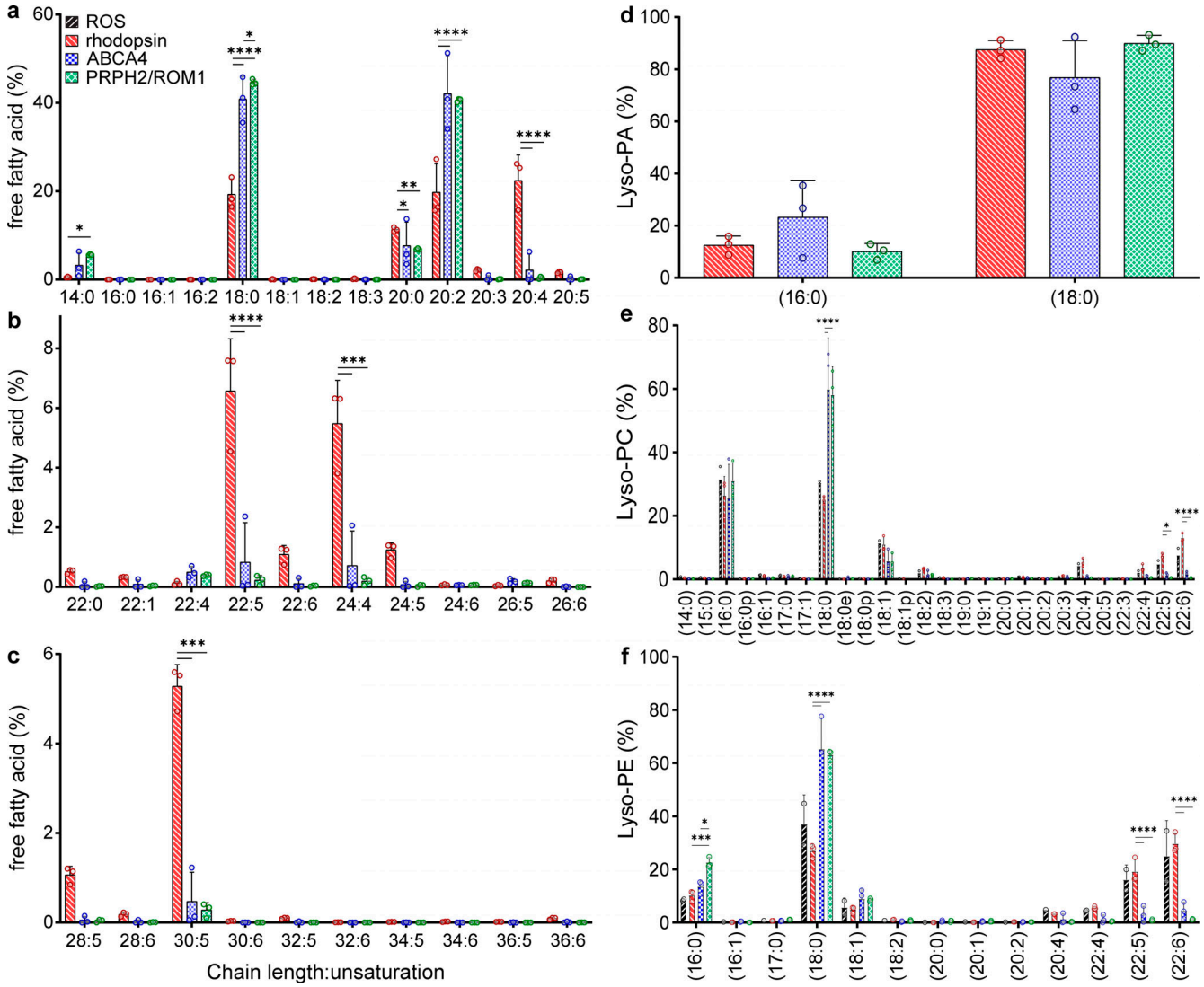

Figure S4. **Every detected species of FFA and Lyso-PL, relative to total species of each class. (a–f)** Every detected species of FFA and lyso-PL that copurified with each sample is shown as a percentage of each respective class (class noted on y axis). Total ROS: black forward stripe; rhodopsin: red backward stripe; ABCA4: blue checker; PRPH2/ROM1: green diamond. The number of measurements for each sample of each species varies, as noted by the individual data points for each bar (open circles). Percent composition was calculated for each sample by dividing the area under the curve for each species in a class by the total area under the curve for that class, measured via LC/MS after correction for variations in internal standard area, sample mass, and sample injection volume. Statistics were determined using two-way ANOVA with Tukey's multiple comparisons post hoc test. Statistical significance values are indicated as follows: *, $P < 0.05$; **, $P < 0.01$; ***, $P < 0.001$; ****, $P < 0.0001$.

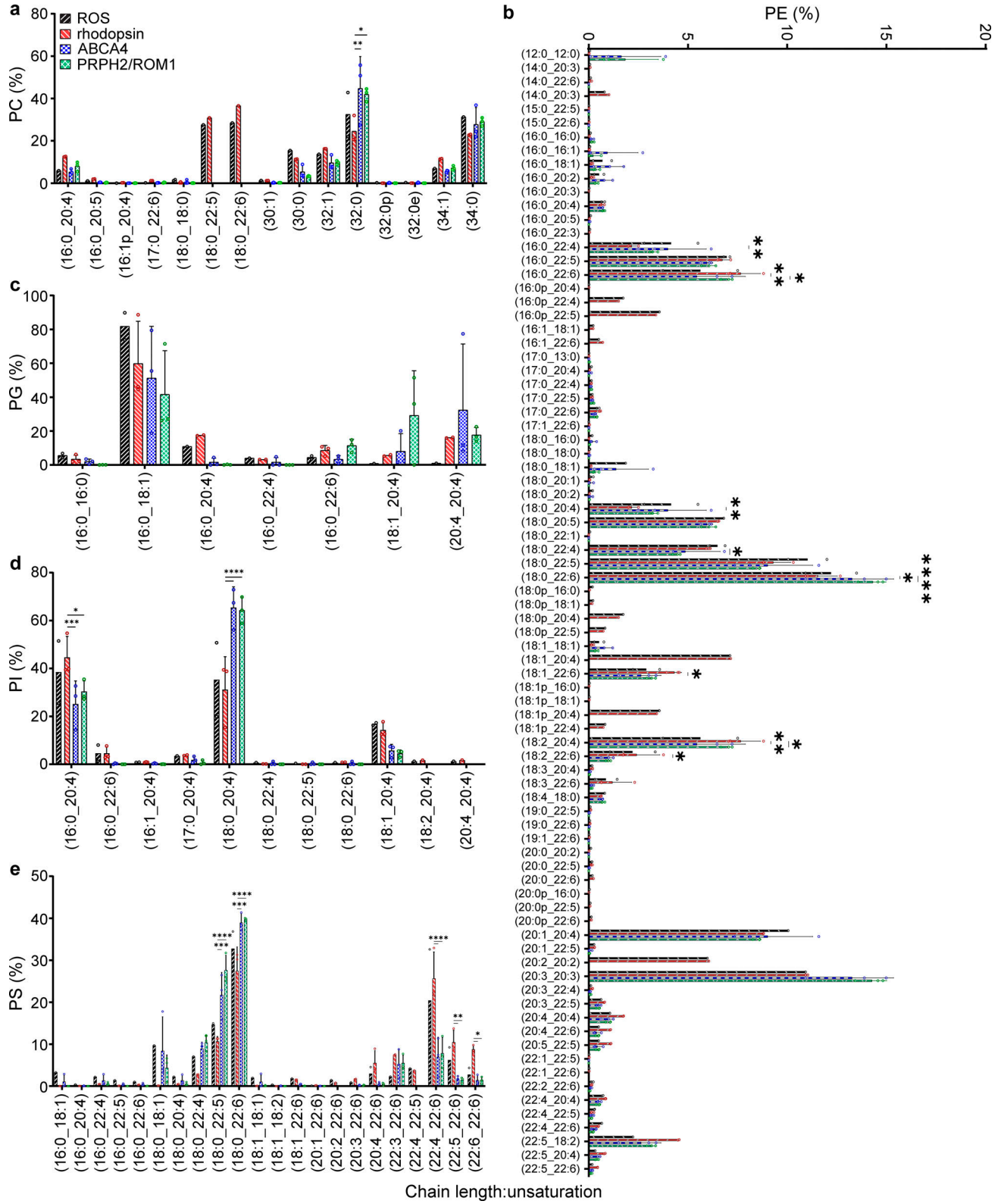

Figure S5. **Every detected species of phospholipid, relative to total species of each class. (a–e)** Every detected species of phospholipid that copurified with each sample is shown as a percentage of each respective class (class noted on y axis). Total ROS: black forward stripe; rhodopsin: red backward stripe; ABCA4: blue checker; PRPH2/ROM1: green diamond. The number of measurements for each sample at each species varies, as noted by the individual data points for each bar (open circles). Percent composition was calculated for each sample by dividing the area under the curve for each species in a class by the total area under the curve for that class, measured via LC/MS after correction for variations in internal standard area, sample mass, and sample injection volume. Statistics were determined using two-way ANOVA with Tukey's multiple comparisons post hoc test. Statistical significance values are indicated as follows: *, P < 0.05; **, P < 0.01; ***, P < 0.001; ****, P < 0.0001. PI, phosphatidylinositol.